Using Local Infrasound to Estimate Seismic Velocity and Earthquake Magnitudes

Kenneth A. Macpherson*[1], David Fee[1], Juliann R. Coffey[1], and Alex J. Witsil[1]

ABSTRACT

Earthquake ground motions in the vicinity of receivers couple with the atmosphere to generate pressure perturbations that are detectable by infrasound sensors. These so-called local infrasound signals traverse very short source-to-receiver paths, so that they often exhibit a remarkable correlation with seismic velocity waveforms at collocated seismic stations, and there exists a simple relationship between vertical seismic velocity and pressure time series. This study leverages the large regional network of infrasound sensors in Alaska to examine local infrasound from several light to great Alaska earthquakes. We estimate seismic velocity time series from infrasound pressure records and use these converted infrasound recordings to compute earthquake magnitudes. This technique has potential utility beyond the novelty of recording seismic velocities on pressure sensors. Because local infrasound amplitudes from ground motions are small, it is possible to recover seismic velocities at collocated sites where the broadband seismometers have clipped. Infrasound-derived earthquake magnitudes exhibit good agreement with seismically derived values. This proof-of-concept demonstration of computing seismic magnitudes from infrasound sensors illustrates that infrasound sensors may be utilized as proxy vertical-component seismometers, making a new data set available for existing seismic techniques. Because single-sensor infrasound stations are relatively inexpensive and are becoming ubiquitous, this technique could be used to augment existing regional seismic networks using a readily available sensor platform.

KEY POINTS

- This study converts recordings of local infrasound to vertical seismic velocity.
- We show that earthquake magnitudes can be estimated from infrasound recordings.
- Infrasound can recover clipped seismic waveforms and can be used as a proxy vertical seismic channel.

INTRODUCTION

When the surface of the earth shakes or rapidly deforms in response to an earthquake, the motion induces pressure perturbations in the atmosphere and generates long-period acoustic waves known as infrasound. Earthquakes generate infrasound in three distinct ways. Large static and dynamic displacements in the near-source region couple with the atmosphere to produce epicentral infrasound (Donn and Posmentier, 1964; Kim *et al.*, 2004; Yang *et al.*, 2021). As seismic waves propagate between source and receiver, they interact with topographic structure, inducing it to radiate secondary or diffracted infrasound (Arrowsmith *et al.*, 2012; Shani-Kadmiel *et al.*, 2018; Johnson *et al.*, 2020). Finally, local infrasound is generated by vertical ground motion in the vicinity of the receiver.

Infrasound phases are generally identifiable from their travel times. Local infrasound, with its negligible source-to-receiver path arrives first, is well separated from epicentral infrasound arrivals, which have long paths from the epicentral region to the receiver. This is because seismic wavespeeds are generally an order of magnitude faster than sound speeds, so that ground motions will occur at receivers before epicentral infrasound arrivals even at small epicentral distances. Diffracted infrasound from source regions between the epicenter and receiver will arrive between local and epicentral infrasound. However, diffracted arrivals may occur following epicentral arrivals, depending on the source–receiver distance to the diffracted infrasound radiator (Che *et al.*, 2021). These travel-time differences between the three earthquake infrasound phases imply that local infrasound recordings are unlikely to be contaminated by later arrivals. The local infrasound source zone can be thought of as a

1. Wilson Alaska Technical Center, Geophysical Institute, University of Alaska Fairbanks, Fairbanks, Alaska, U.S.A., https://orcid.org/0000-0002-5521-6912 (KAM); https://orcid.org/0000-0002-0936-9977 (DF); https://orcid.org/0000-0002-9686-4326 (JRC); https://orcid.org/0000-0003-0200-0074 (AJW)

*Corresponding author: kamacpherson@alaska.edu

Cite this article as Macpherson, K. A., D. Fee, J. R. Coffey, and A. J. Witsil (2023). Using Local Infrasound to Estimate Seismic Velocity and Earthquake Magnitudes, *Bull. Seismol. Soc. Am.* **113**, 1434–1456, doi: 10.1785/0120220237

circular area with a radius of four times the wavelength of the dominant seismic period (Cook, 1971). This means that for a 10 s surface wave with a group velocity of 3.5 km/s, the source zone has a radius of 140 km. Therefore, a secondary infrasound radiator at the source boundary would require around 7 min travel time to arrive at the receiver and would arrive after the most vigorous local shaking.

Both epicentral and diffracted infrasound have been investigated for their potential to constrain earthquake source parameters. Epicentral infrasound has been studied by Arrowsmith *et al.* (2012) to understand the ground-to-air coupling mechanism and how it may relate to earthquake source parameters, although this is difficult due to the dynamic nature of the atmosphere and long source-to-receiver atmospheric path. Backprojection of epicentral infrasound has been used to estimate the shaking intensity of the 2010 Haiti earthquake due to the paucity of seismometers in the epicentral region (Shani-Kadmiel *et al.*, 2018). Yang *et al.* (2021) used an earthquake doublet in Alaska to show that the energy from diffracted infrasound exhibits similar spatial distributions to seismic energy, indicating that it is sensitive to the seismic source.

The very short source–receiver path of local infrasound, on the order of centimeters to tens of kilometer, results in a remarkable correlation in waveform shape between the vertical seismic velocity and the infrasound pressure record, particularly at surface-wave periods, which are typically longer than around 10 s. Donn and Posmentier (1964) analyzed the group velocities of pressure perturbations induced by local Rayleigh waves following the 1964 Alaska earthquake to show that the pressure waves conform to standard oceanic and continental dispersion curves. The similarity of local infrasound recordings to vertical ground motion has also been exploited to extract a transfer function from seismic to infrasound signals at sites with collocated infrasound sensors and broadband seismometers (Kim *et al.*, 2004; Watada *et al.*, 2006; Fee *et al.*, 2023). If the response of the seismometer and local atmospheric conditions are known, the transfer function may be used to calibrate the infrasound sensor. This technique has added utility for wind–noise reduction system (WNRS) equipped infrasound stations, where the actual instrument response is known, but the response of the WNRS is less understood.

The purpose of this study is to exploit the similarity between local infrasound and vertical seismic velocity to use infrasound sensors as proxy ground-motion instruments. By leveraging the simple relationship between vertical ground motion and pressure time series of collocated seismoacoustic stations, we estimate seismic velocity from local infrasound observations. Because the technique results in a waveform that is equivalent to a broadband recording of vertical velocity, we give examples of the utility of this unique data type. First, we show how local infrasound from collocated stations may be employed to recover the vertical seismic time series at stations where the broadband seismometer has clipped. Then, we show several examples of how local infrasound converted to vertical seismic velocity may be used to scale earthquake magnitudes. Magnitudes are computed for eight light-to-great earthquakes (**M** 3.7–8.2) in the Alaska region that were recorded on the hundreds of infrasound sensors in the state (see (Lay and Wallace, 1995) for earthquake categories). The effectiveness of the technique demonstrates that infrasound stations may be used as a proxy for broadband seismometers when the conventional seismic recordings have gone off scale or are otherwise not available. The purpose of these examples is not to exhaust the utility of local infrasound for earthquake source scaling but to give a proof of concept of the potential for infrasound to be used as a proxy for vertical seismic recordings. We also note that a companion study is published in this issue by Fee *et al.* (2023) that uses local infrasound recordings of large Alaska earthquakes and collocated broadband sensors to characterize the frequency response of infrasound sensors.

Infrasound sensors and seismicity in the Alaska region

Alaska is an ideal region for observing local infrasound due to its high seismicity rate and ubiquity of infrasound sensors. Several networks operate infrasound stations and/or arrays in the state, including the Alaska Earthquake Center (network AK), the Alaska Volcano Observatory (network AV), the Global Seismographic Network (GSN; network IU), and the International Monitoring System (IMS; network IM; Scripps Institution of Oceanography, 1986; Alaska Earthquake Center, University of Alaska Fairbanks, 1987; Alaska Volcano Observatory/USGS, 1988). However, a relatively dense, regional-scale network was established beginning in 2014 with the deployment of the USArray Transportable Array (TA), where most stations were equipped with a single Hyperion IFS-4132 infrasound sensor (Melter *et al.*, 1999; IRIS Transportable Array, 2003; Busby and Aderhold, 2020). Although the TA ceased operating in Alaska in 2021, over 100 of the former TA stations have been adopted into the permanent regional networks AK and AV. All former TA infrasound sensors are collocated with a broadband seismometer, either a Streckeisen STS-5A or Nanometrics Trillium 120 (Busby and Aderhold, 2020). The TA and former TA infrasound sensors are not equipped with WNRS, and were located to conform to the TA geographic planned grid, so that may experience high levels of wind-induced noise (Macpherson *et al.*, 2022). About 11 TA stations were adopted into the AV network. These stations are near volcanic centers and consist of similar equipment as the other TA stations. Other existing AV stations had similar installation configurations but generally consist of Chaparral Model 64 sensors and a few have modest WNRS systems. The IMS array in Alaska, I53US, is an eight-element array equipped with Hyperion 5313/A sensors. The array has an approximately 2 km aperture, and each element is equipped with a WNRS. A GSN

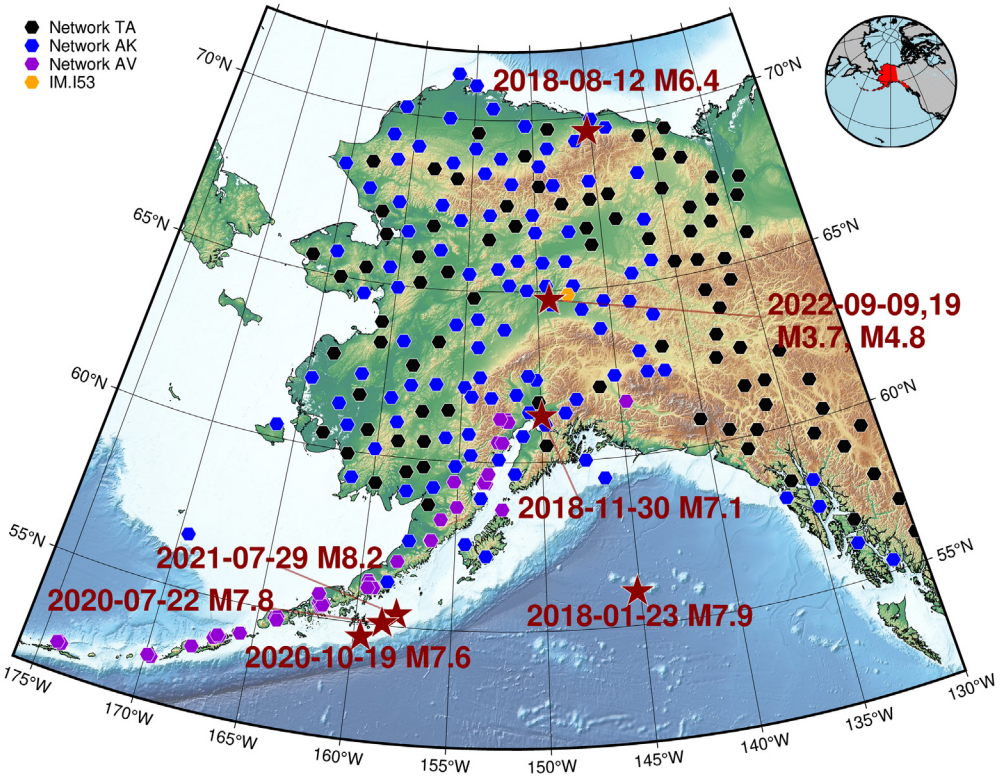

Figure 1. Map of the Alaska region showing infrasound stations and earthquakes considered in this study. Not all stations were operational contemporaneously, but all were operational for some period between 2018 and October 2022. Inset at top right indicates the position of Alaska at a global scale. The color version of this figure is available only in the electronic edition.

broadband seismic station, COLA, is essentially collocated with the H1 element of I53US. This station is equipped with a Streckeisen STS-5A broadband seismometer in a 10 m deep borehole. A map showing the distribution of infrasound-equipped stations in the Alaska region is shown in Figure 1.

Since 2018, the state of Alaska has experienced five earthquakes in excess of magnitude 7, providing several seismic sources that produced region-wide local infrasound at times when large numbers of infrasound stations were available. The event dates, magnitudes from National Earthquake Information Center (NEIC), and epicenters are shown in Figure 1. Throughout this article, we refer to NEIC-published magnitudes generically as "**M**." However, for all event considered in this study with **M** ≥6.4, the NEIC magnitude is from a centroid moment tensor derived by inverting the *w*-phase, is denoted as M_{ww}, and uses stations from local out to the maximum of 90° epicentral distance. The NEIC magnitudes for the two smaller earthquakes considered in the study are local magnitudes (M_L) computed using the regional network. The events considered here represent a diversity of source types: shallow crustal, subduction zone interface, intraplate and intraslab, and intermediate depth events. Subsequently, we provide some details on the eight events considered in this study.

The 23 January 2018, Kodiak earthquake struck the Gulf of Alaska and was a result of complex intraplate faulting of the Pacific plate. With a magnitude of 7.9 and depth of around 10 km, this event prompted a tsunami warning and was felt throughout the state of Alaska. The mechanism was primarily strike slip on a complex set of faults, with backprojection analysis indicating rupture of at least four faults with strikes both to the northwest and east (Krabbenhoeft *et al.*, 2018; Lay *et al.*, 2018; Ruppert *et al.*, 2018). The **M** 6.4 Kaktovik event was the largest earthquake of the instrumental age to occur in the North Slope area of Alaska and occurred on 12 August 2018. It was a result of crustal strike-slip faulting on a complex set of at least three easterly striking faults at a depth of around 10 km (Xu *et al.*, 2020). The **M** 7.1 Anchorage earthquake struck densely populated Southcentral Alaska on 30 November 2018. This earthquake prompted tsunami warnings despite its onshore location, was widely felt, and caused considerable damage. The event was a result of reverse faulting within the subducting Pacific slab (West *et al.*, 2020). Damage was limited somewhat due to the intermediate depth (43 km) of the event.

Three earthquakes with **M** > 7.0 struck in the vicinity of the subduction zone south of the Alaska peninsula between July 2020 and July 2021. An **M** 7.8 event struck near Simeonof Island south of Perryville, Alaska, on 22 July 2020. This event was likely a result of thrust faulting at the subduction interface at a depth of around 28 km and was tsunamigenic. This event was notable due to its location in a seismic gap that had not produced a sizable earthquake since 1917 (Crowell and Melgar, 2020; Xiao *et al.*, 2021). A few months later, on 19 October 2020, an **M** 7.6 earthquake occurred approximately 80 km to the southwest of the 22 July 2020 epicenter, south of the village of Sand Point, Alaska. This event was a result of strike-slip intraslab faulting within the downgoing Pacific plate and is considered an aftershock of the July event. The magnitude is large for a strike-slip mechanism not situated in an outer rise area and produced a tsunami with similar amplitudes to the **M** 7.8 event (Herman and Furlong, 2021). On 29 July

2021, a great earthquake with a magnitude of **M** 8.2 struck east of the **M** 7.8 and 7.6 epicenters near the Alaska community of Perryville. This earthquake had a thrust mechanism and was a result of a rupture at the interface of the North American and Pacific plates (Elliott *et al.*, 2022).

Finally, we consider two light earthquakes that occurred within 10 days of each other near the Alaska village of Minto. The first occurred on 9 September 2022 and had a local magnitude (M_L) of 3.5 with a depth of around 16 km. It was followed by an M_L 4.9 event 1.5 km to west on 19 September 2022 with a depth of around 19 km. Both of these events were a result of crustal strike-slip faulting (A. McPherson, personal comm., 2022). The M_L 4.9 was clearly felt in the city of Fairbanks, around 60 km away.

These eight events span a wide variety of locations, tectonic regimes, source mechanism, and magnitudes. The greater than magnitude six events were well recorded on both seismic and infrasound in the Alaska region out to at least 1500 km, whereas the two Minto earthquakes were well recorded locally on the I53US array, providing a robust data set for the investigation of local infrasound.

METHODS

Our goal is to use local infrasound observations to estimate vertical seismic velocity and illustrate how such estimates have utility as a proxy for seismic data, including computing earthquake magnitudes. To do this, we leverage the simple relationship between pressure change and vertical ground velocity given by

$$\Delta P = \rho c v_z, \tag{1}$$

in which ΔP is the perturbation pressure, ρ is the air density, c is the speed of sound in the air, and v is the vertical ground velocity (Donn and Posmentier, 1964; Kim *et al.*, 2004). This expression is defined for planar wave generation, and this assumptions holds due to the order of magnitude difference between acoustic and seismic wavespeeds. The vertical component of the plane acoustic wave matches that of the seismic surface wave at the air–ground interface. The angle of propagation is a function of the wavespeeds and is approximated by $\arctan(c/c_0) \approx \arctan(1/10)$, in which c is the sound speed, and c_0 is the seismic wavespeed (Cook, 1971). This means the angle is ≤6°, so that any horizontal component is negligible. By assuming a constant air density of 1.225 kg/m^3, we estimate the vertical seismic velocity from the local infrasound perturbation simply as follows:

$$v_z(t) = \frac{\Delta P(t)}{\rho c}, \tag{2}$$

for time t. Many of the infrasound stations in Alaska are equipped with meteorologic sensors; so if outside temperatures are available at a particular station, we approximate the sound speed as $c = 331.3 + 0.606T_{avg}$ m/s, in which T_{avg} is the average temperature in Celsius from one hour of data beginning at the start of the recording. If no temperature data are available at a station, we set the sound speed to 334 m/s, corresponding to an air temperature of 5°C. The acoustic parameters of sound speed and density are assumed to be constant over the entire acoustic propagation path. Although there are certainly variations, these should be minimal over the short centimeter to tens of kilometer source–receiver offsets of local infrasound. Our procedure for estimating vertical seismic velocity from local infrasound consists of deconvolving the instrument response from the infrasound time series so that we have a pressure record in Pascals (Pa) and then converting the pressure time series to meters per second via equation (2). We refer to data thus converted as converted local infrasound (CLI).

An example of this procedure is shown in Figure 2 using the local infrasound generated by the 19 October 2022 **M** 7.6 Sand Point earthquake. Figure 2a shows the vertical ground-motion trace from the broadband seismometer at station F18K, located at an epicentral distance of ≈1300 km. The trace in Figure 2b is the pressure record from the infrasound sensor at the same station.

For both seismic and infrasound, we removed the instrument response and applied a high-pass filter with a 20.0 s corner to eliminate background pressure fluctuations in the infrasound (Watada *et al.*, 2006). The remarkable correlation between the seismometer-recorded ground motion and the local infrasound is clearly apparent in Figure 2c. Although local infrasound is often described as resulting from the vertical ground motion induced by the Rayleigh wave (e.g., (Donn and Posmentier, 1964), body-wave phases are clearly visible in the infrasound time series—a phenomenon previously noted by Kim *et al.* (2004) and by Fee *et al.* (2023) (see this issue). The *P*, *S*, and first surface-wave arrivals, as estimated using the IASP91 velocity model and a surface-wave group speed of 3.5 km/s, are indicated by vertical lines in the figure. The brown trace in Figure 2c is the CLI estimate using the procedure described earlier, with a sound speed of 330 m/s. Cross correlating the seismic recording with the CLI results in a correlation coefficient of 0.98. The CLI amplitudes do not match the seismic amplitudes exactly. Because we have an observation of temperature at this site, we investigated the effects of modifying the air density values. We found that by increasing the density considerably, we were able to achieve closer agreement in the amplitudes, but that the differences are negligible for reasonable values of density.

To demonstrate the efficacy of using CLI to calculate seismic source parameters, we compute the source magnitude for the eight earthquakes considered in the study. Because we consider earthquake sizes from light to great, more than one type of magnitude estimator is required. For the three crustal earthquakes with magnitude less than 6.8, we compute the vertical local magnitude (M_{lv}), which is appropriate for earthquakes of this size. All the remaining events have magnitudes in excess of

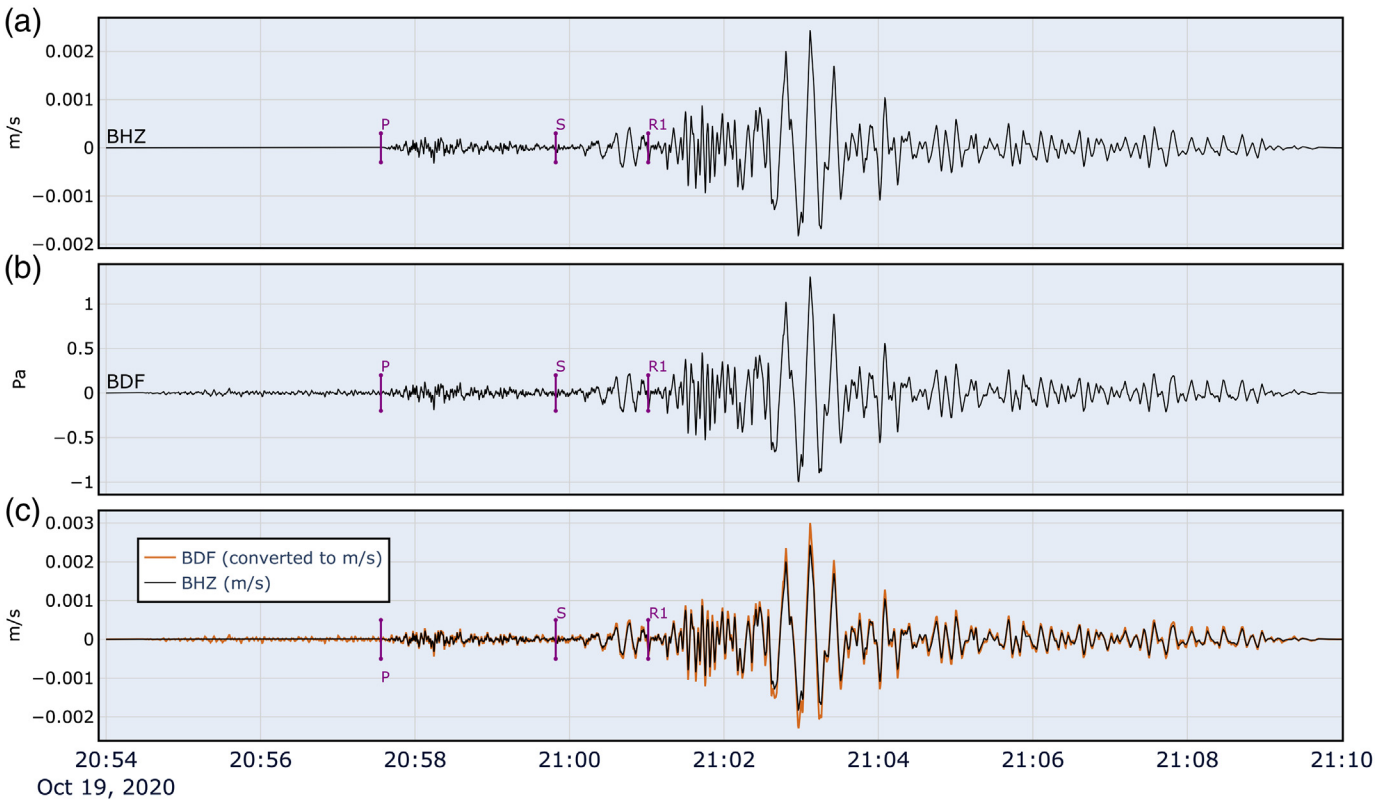

Figure 2. The **M** 7.6 Sand Point earthquake recorded at station F18K. (a) Deconvolved vertical seismic channel. (b) Deconvolved infrasound pressure record. (c) Vertical seismic trace in black, along with the infrasound converted to seismic velocity in brown. Vertical lines labelled "*P*" and "*S*" denote the *P*- and *S*-wave arrivals, respectively, as estimated using the IASP91 velocity model (Kennett and Engdahl, 1991). The vertical line labelled "*R*1" denotes the first surface-wave arrival, assuming a group velocity of 3.5 km/s. The color version of this figure is available only in the electronic edition.

7, so we use a broadband surface-wave magnitude estimator for them. Both of these magnitude estimate techniques are discussed subsequently.

Vertical local magnitude (M_{lv})

The local magnitude is the modern variant of of the original Richter magnitude, in which maximum amplitudes, usually of an *S* wave, are read from modern instruments adjusted to utilize the response of a Wood–Anderson seismograph (Richter, 1935). Typically, horizontal components are used; but the M_{lv} variant uses the vertical component only and is thus well suited for use with CLI, for which the infrasound sensor acts as a proxy for a vertical seismic channel. There exists a plethora of local magnitude formulas, but we use the ObsPy magnitude estimation tool, which is an implementation of the Bakun and Joyner (1984) version (Beyreuther *et al.*, 2010; Krischer *et al.*, 2015). The formula is given by

$$M_L v = \log A + 1.11 \log r + 0.00189 r - 2.09, \qquad (3)$$

in which r is the epicentral distance, usually with $r \leq 600$ km, and A is the maximum amplitude measured on a vertical displacement waveform that has been convolved with the response of a Wood–Anderson instrument. Because the ObsPy tool expects a waveform that has not had the instrument response removed, after converting pressure records to velocity, we band-pass filtered between 1.0 and 5.0 Hz and convolve the converted pressure record with the response of either the collocated seismometer, if available, or a nearby seismometer. The ObsPy tool will then remove the provided instrument response before simulating the Wood–Anderson response. We then measure the maximum peak-to-trough amplitude (in counts) and peak-to-trough period, and pass these values as well as the seismometer response to the ObsPy tool. The tool performs the Wood–Anderson simulation and computes the magnitude. To compute source–receiver offsets, we use origin information from the Advanced National Seismic System (ANSS) Composite Catalog and use the ObsPy geodetics library to compute distance (Beyreuther *et al.*, 2010; U.S. Geological Survey, 2017). We estimate *P*-wave arrival time from the ANSS origin time and the IASPA91 velocity model (Kennett and Engdahl, 1991). We window data from origin time to 3 min following the *P* arrival for the the two interior Alaska earthquakes recorded on I53US. For the 12 August 2018 Kaktovik earthquake, we window each station from 2 min prior to *P* arrival to 5 min following. It is well known

that the local magnitude saturates around **M** 6.8, limiting its use in this study to the **M** 3.7, 4.9, and 6.4 earthquakes.

Broadband surface-wave magnitude (M_s_BB)

The broadband surface-wave magnitude (M_s_BB) is an ideal method for estimating the magnitude of the five magnitude greater than seven earthquakes using CLI. The M_s_BB estimator does not saturate, except for the largest earthquakes, relies on the vertical component of velocity only, and is valid for a large range of distances, including offsets as small as 2° (Kárník *et al.*, 1962; Bormann *et al.*, 2009; Bormann and Dewey, 2012). In addition, the NEIC-reported origins of all the five events have source depths less than 60 km, making them suitable for surface-wave magnitude analysis. The magnitude is given by

$$M_s\text{\_BB} = \log\left(\frac{V_{\max}}{2\pi}\right) + 1.66\log(\Delta) + 3.3, \qquad (4)$$

in which $V_{\max}$ is the maximum zero-to-peak amplitude measured on the vertical component of a broadband velocity seismogram, and Δ is the epicentral distance in degrees. Our procedure for calculating M_s_BB consists of converting the infrasound pressure record to velocity, band-pass filtering between 3 and 60 s, and measuring the zero-to-peak amplitude. As in our M_{lv} calculations discussed earlier, source–receiver offsets are computed from the ANSS origin information. We compute the window for the amplitude measurement starting with the *P* arrival until 10 min past the estimated surface-wave arrival, assuming a group velocity of 3.5 km/s. All network magnitudes are computed by finding the 12% trimmed mean of all available magnitudes.

RESULTS

In this section, we provide examples of the appropriateness and utility of CLI. First, we show how local infrasound recordings can be used to recover seismic waveforms that have clipped. We then show results of using CLI to scale earthquake magnitudes.

Recovering clipped waveforms at collocated sites

A problem for many seismological algorithms that utilize broadband data is the presence of amplitudes that exceed the dynamic range of the instrument—a phenomenon known as clipping (Kleckner *et al.*, 2022). If peak amplitudes are not reliably represented in a waveform, then the data are not useful for tasks such as estimating earthquake magnitude. Clipping may also occur when the instruments response becomes nonlinear, even if its dynamic range is not exceeded. Strong-motion seismic instruments and high-rate Global Positioning System sensors are able to record large ground motions without clipping, although they record in acceleration and displacement, respectively.

Because of the onshore, Southcentral Alaska location of the 2018-11-30 M7.1 Anchorage earthquake, there were many broadband stations located in the near-source region (see Fig. 1). This resulted in a large number of broadband waveforms that clipped following the event. The TA station RC01 provides a good illustration of the loss of information that occurs from clipping. It is located at around 36 km from the M 7.1 epicenter. The raw waveform from the vertical channel is shown in the top panel of Figure 3a. It has clearly gone off scale, as indicated by the "squared-off" appearance of the extreme values, as well as experienced nonlinear effects, probably from tilting. This channel was also clipped by the M 5.8 aftershock that occurred about 6 min later. The middle panel in Figure 3a shows the raw data from the collocated infrasound sensor at RC01. The local infrasound for both the mainshock and the aftershock are well recorded in the raw infrasound. Comparing the CLI with the deconvolved seismic data (bottom panel of Fig. 3a), it is clear that the CLI waveform is useful for algorithms requiring an amplitude measurement, whereas the seismic channel is clearly compromised. Also plotted in the bottom panel is the integrated waveform for the collocated Episensor accelerometer at this station, the maximum amplitudes of which are largely in agreement with the CLI.

To determine the number of broadband stations that clipped following the **M** 7.1 event, we examined the maximum value in counts of all available regional raw seismic waveforms following the *S*-wave arrival. We estimate the dynamic range of the digitizer as 2^{N-1}, in which N is the the digitizer bit-weight. Assuming that all digitizers in the AK, TA, and AV networks are 24 bit, we conclude that a waveform has clipped if it contains raw values that are $\geq 2^{23}$. Using this threshold, we determined that 35 out of the available 306 regional broadband instruments clipped (see Fig. 3b). Clipped stations cluster around the epicenter as expected, but somewhat surprisingly, clipping occurs out to an epcientral distance of 347 km, and often clipped stations are in close proximity to stations that stayed on scale, probably as a result of site effects. Of the 35 clipped broadband stations, 15 have collocated infrasound sensors. Figure 4 shows the 15 clipped seismic waveforms in black, along with the collocated CLI recordings in brown.

Because the pressure perturbation induced by the vertical ground motion is relatively small relative to the dynamic range of the sensor, the CLI signal is on scale for all the 15 stations. This allows for the recovery of a vertical ground-motion waveform that has not been compromised by clipping. There are much larger amplitudes represented in the CLI compared to the deconvolved seismic waveforms. Even station K24K, at almost 350 km epicentral distance, exhibits clipped amplitudes that are fully available in the CLI. Although the CLI recordings generally have larger amplitudes than the clipped seismic, stations CAPN, CUT, and HARP are clear exceptions. Upon investigation, we discovered that the infrasound sensors at CAPN and CUT were installed as part of an upgrade associated with the deployment of the TA. Therefore, they do not conform to the standard TA hut design, for which the infrasound is ported to the atmosphere via a diffuser on the side of the hut

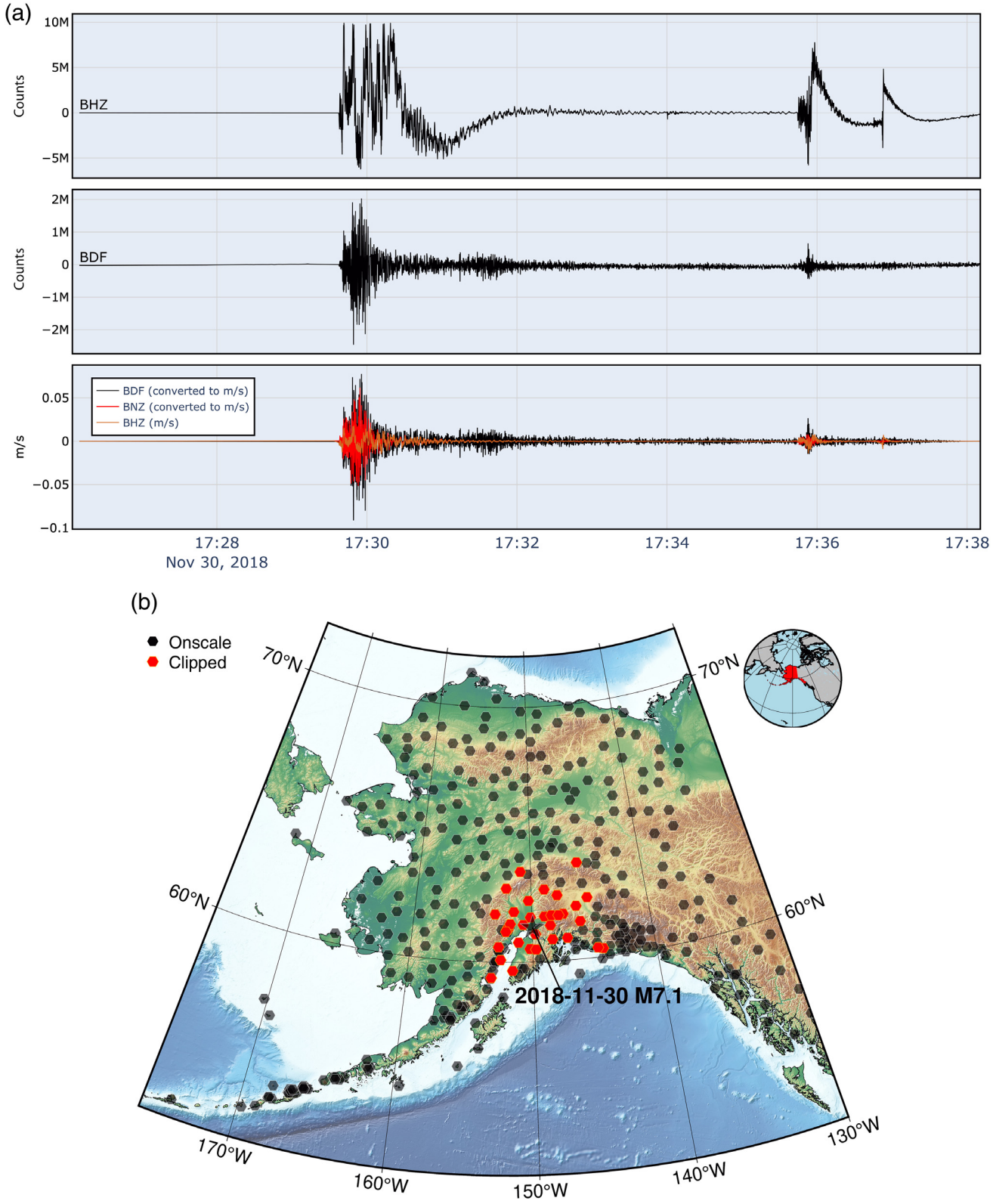

Figure 3. (a) The 30 November 2018 **M** 7.1 Anchorage earthquake recorded at station RC01. Top panel shows the raw seismic data from the vertical channel, whereas the middle panel shows the raw pressure record from the collocated infrasound sensor. The bottom panel shows the seismic data with the instrument response removed in brown, whereas the converted local infrasound (CLI) recording is shown in black. The integrated waveform from a collocated accelerometer is shown in red. (b) Map of the available regional broadband seismic stations on 30 November 2018, denoted by hexagons. The stations that were determined to have clipped waveforms are shown as red hexagons, whereas stations that remained on scale are shown in gray. Inset at top right indicates the position of Alaska at a global scale. The color version of this figure is available only in the electronic edition.

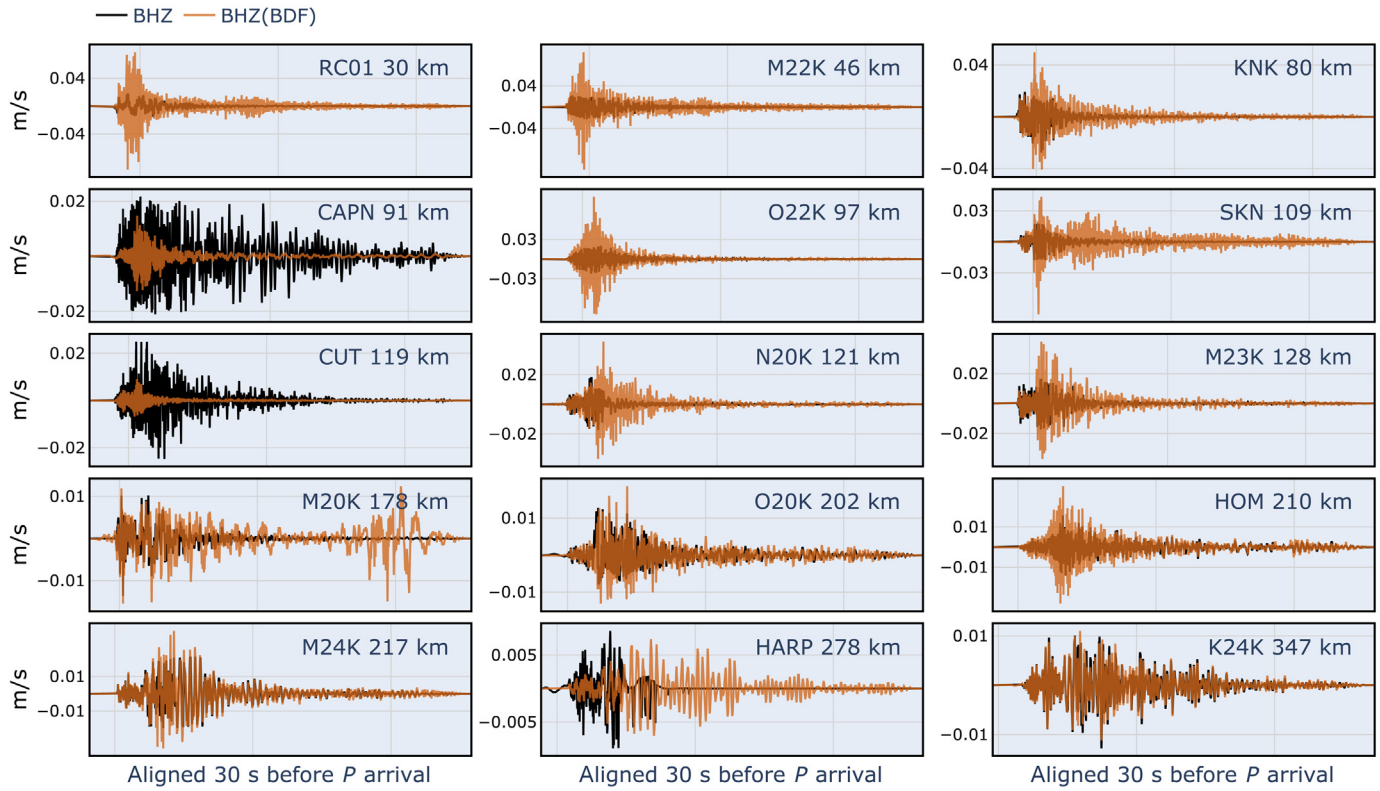

(Busby and Aderhold, 2020). At CAPN and CUT, the sensor resides inside a cooler, and it has been determined that the sensor was not properly ported to the atmosphere and has an atypical response (Macpherson *et al.*, 2022; Fee *et al.*, 2023). The physical cause of the response issue at HARP has not been determined, but the issue was identified by a seismoacoustic calibration techniques presented in the current issue (Fee *et al.*, 2023). Although this means that the local infrasound recorded at these two stations are compromised, it does indicate that comparing CLI to collocated seismic recordings has potential as a data quality tool.

To illustrate how clipping can affect magnitude estimates and how these may be improved by incorporating CLI, we computed the M_{lv} for the **M** 7.1 Anchorage earthquake from the 12 stations shown in Figure 3 that do not have known response issues. Although the magnitude of this event is at or above the saturation level for M_{lv}, we chose this estimator for comparing magnitudes between clipped seismic and CLI due to the fact that the passband required for M_s_BB limits the effects of clipping. The results for the 12 stations are shown in Table 1. Magnitudes computed from infrasound and seismic data are shown in columns one and two, respectively. Column 3 shows the ratio of of the maximum observed seismic amplitude to the maximum observed infrasound amplitude in the 1–5 Hz passband. As we would expect, all stations have higher magnitude estimates from the unclipped CLI than from the compromised seismic, with the exception of K24K. This station does not appear to have been clipped severely (Fig. 3), so that magnitudes from seismic and CLI are similar.

Figure 4. All collocated broadband and infrasound stations with clipped seismic following the 30 November 2018 **M** 7.1 earthquake. For each station, the vertical velocity from the broadband seismometer is shown in black, whereas the vertical velocity from the infrasound sensor is shown in brown. Station name and epicentral distance is indicated above each trace. Waveforms have been filtered with a 2 s high-pass filter to remove background pressure fluctuations in the infrasound. The infrasound sensors at stations CAPN, CUT, and HARP have known response issues. The color version of this figure is available only in the electronic edition.

Magnitude of a light earthquake recorded on an infrasound array

Local infrasound from the 19 September 2022 M 4.9 earthquake was well recorded on the IMS array I53US at about 62 km epicentral distance. We converted the local infrasound recording of this earthquake to seismic velocity at all eight array elements and then convolved the results with the instrument response from the seismometer at COLA. The waveforms from I53US and COLA, along with the picked peak-to-trough amplitude and computed earthquake magnitude for each element, are shown in Figure 5b. The single-station magnitude computed from the vertical channel of COLA is 4.84, resulting in good agreement with the **M** 4.9 magnitude computed by the Alaska Earthquake Center. The trimmed mean magnitude from the eight elements of the I53 array is 4.98. There are considerable differences in maximum amplitude and resulting magnitudes between the elements, with a standard deviation of approximately 0.28 magnitude units. The H1 element exhibits the highest magnitude at 5.54, whereas H6 is the lowest at

TABLE 1
Magnitude Results for the M 7.1 Anchorage Earthquake from the 12 Stations with Clipped Seismometers and Collocated Infrasound Sensors

Station	M_{lv}, Infrasound	M_{lv}, Seismic	Amplitude Ratio
RC01	6.16	5.38	0.16
M22K	6.50	5.90	0.25
KNK	6.41	6.33	0.82
O22K	7.05	6.47	0.26
SKN	6.50	6.32	0.65
N20K	6.67	6.49	0.67
M23K	6.59	6.51	0.83
M20K	6.57	6.54	0.93
O20K	6.81	6.72	0.80
HOM	7.17	6.82	0.44
M24K	6.92	6.85	0.86
K24K	7.25	7.30	1.13

Three stations were with known response issues are not included. First column shows local magnitude computed from converted local infrasound (CLI), the second column shows local magnitude computed from the clipped seismic waveforms, and the third column shows the seismic to infrasound maximum amplitude ratio.

4.59. We speculate that these large differences over small distances is a result of highly local site conditions at the elements and the relatively high-frequency 1–5 Hz passband, and we expect more consistency across the array at lower frequencies, as demonstrated by a seismoacoustic calibration technique (Fee *et al.*, 2023).

Magnitudes for two large earthquake from a regional infrasound network

In this section, we show detailed results from the computation of network magnitudes from the regional network of infrasound sensors in the Alaska region for two large earthquakes using the broadband surface-wave magnitude estimator. Because of the lack of WNRS on the majority of these stations, and the fact that former TA station were sited without regard to infrasound performance, many of them have high levels of background noise and do not record local infrasound as reliably as the regional seismic network records ground motions (Macpherson *et al.*, 2022). For this reason, we consider only stations with collocated broadband seismometers, and we cross correlate the vertical seismic trace with the CLI. Stations with a greater than 66% correlation are considered to have recorded usable local infrasound and are retained. We also retained stations with clipped seismic waveforms, assuming that, although correlations may be low, there is likely to be a large infrasound signal as a result of the strong ground motion.

Applying this criteria, the 19 October 2020 **M** 7.6 Sand Point earthquake generated well-recorded infrasound at 74 stations. Figure 6a shows a record section of both seismic and CLI waveforms, whereas Figure 6b shows retained stations colored by station magnitude. The 12% trimmed mean magnitude for the 74 stations yields M_s_BB ≈ 7.67—a value similar to the M 7.6 NEIC magnitude. Examination of Figure 6 reveals that there is some spatial bias in the distribution of magnitudes, with station in the Aleutians and southeastern Alaska reporting low values, whereas northern Alaska stations generally report high values. This spatial pattern is present in magnitudes computed from both seismic and CLI, indicating it is likely due to the radiation pattern or local site conditions. The waveform plots show the good agreement between the seismic and CLI. While seismic waveforms are shown for comparison, only CLI time series were used for the M 7.67 magnitude calculation. Using the seismic data alone, we obtain M_s_BB ≈ 7.62, just marginally better than the CLI relative to the NEIC magnitude of 7.6.

The 23 January 2018 Kodiak earthquake generated well-recorded local infrasound at 85 stations. Figure 7a shows both seismic and CLI waveforms, whereas Figure 7b shows retained stations colored by station magnitude. The 12% trimmed mean magnitude from these 85 stations using CLI yields M_s_BB ≈ 7.78. This value is a modest underestimate of the **M** 7.9 NEIC magnitude. Our magnitude estimate using seismic is actually poorer for this event, at M_s_BB ≈ 7.69.

To summarize our magnitude results, we show our computed magnitudes for all eight events in Table 2. The table lists the 12% trimmed means computed from both seismic data and CLI data, and the number of stations used in each trimmed mean. There is generally broad agreement between our infrasound-derived magnitudes and the catalog values from the NEIC. However, there is even better agreement between our magnitudes computed with infrasound data and with seismic data, indicating the efficacy of CLI as a proxy for a vertical seismic channel. All waveforms and amplitude picks used to compute magnitudes for this study are shown in the Appendix (Figs. A1–A7).

DISCUSSION

The examples given earlier illustrate the potential of CLI data as a proxy for conventional broadband vertical ground-motion recordings. Infrasound may be used to augment available seismic data or if seismic data are compromised, as in the case of clipping, to replace it. Near-source broadband instruments record important information that is often lost to clipping, and considerable effort is made to recover such information (Zhang *et al.*, 2016). The example given earlier for station RC01, at a distance of around 31 km from the 2018 Anchorage earthquake, illustrates how clipping can render a broadband channel unusable for computing magnitudes or other amplitude-dependent source parameters. However, the collocated infrasound sensor allows us to recover the uncompromised vertical seismic velocity (see Fig. 4). This allows for improved magnitude estimates, as we show by computing M_{lv} for the Anchorage earthquake using clipped seismograms and comparing the results to M_{lvi} computed from local infrasound. The results in Table 1 show an improved magnitude

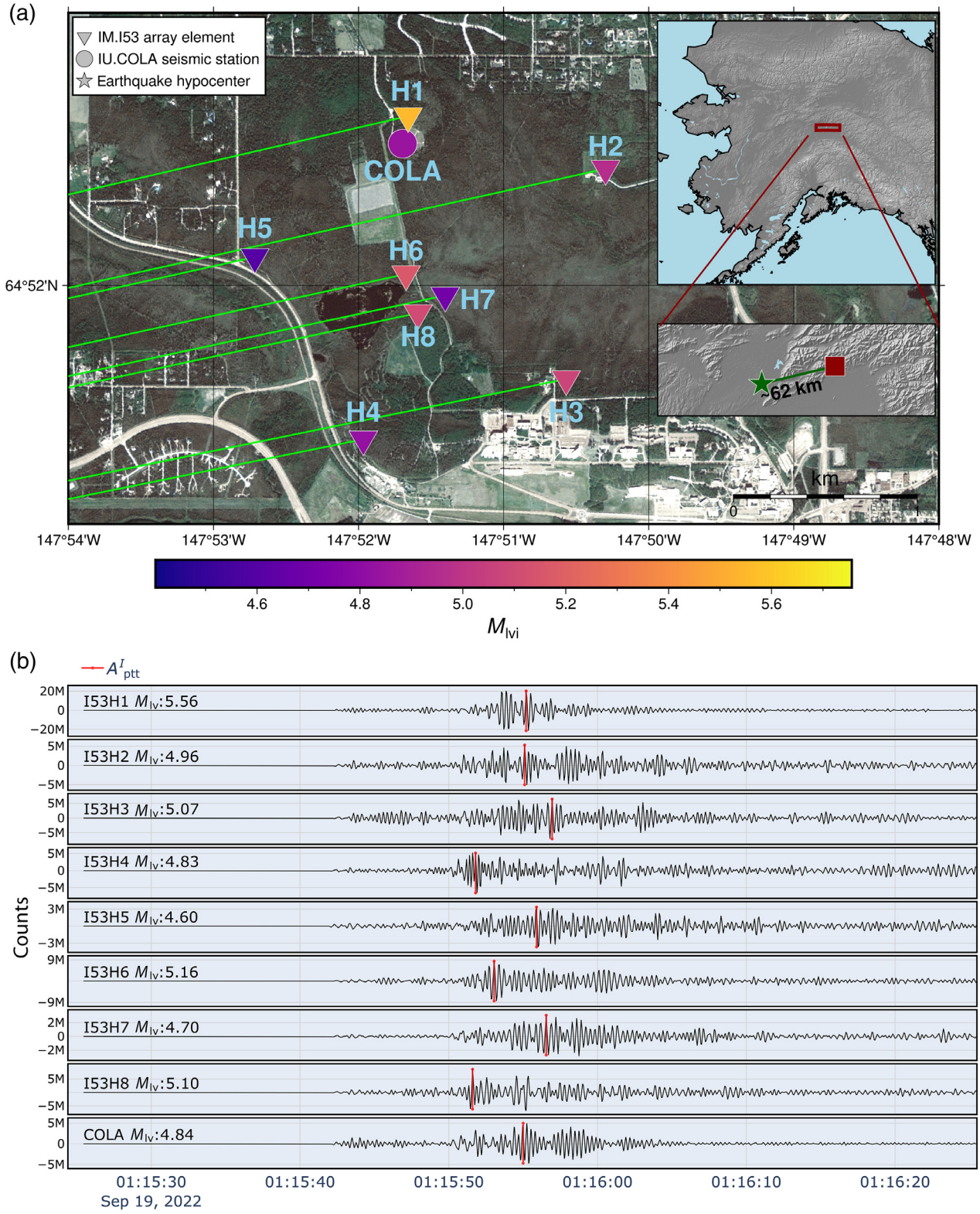

Figure 5. The 19 September 2022 **M** 4.9 Minto earthquake recorded at International Monitoring System (IMS) array I53US and at Global Seismographic Network (GSN) station COLA. (a) Map view of the array, with each element represented by an inverted triangle colored by the station magnitude. The broadband seismic station COLA is denoted by a circle colored by station magnitude. Green lines denote the backazimuth to the epicenter. Insets at right show the regional context of the source and receivers. (b) The waveforms at each infrasound element as well as the seismic station. The maximum peak-to-trough picks are indicated by a vertical red line. Element names and individual station magnitudes are shown above each trace. Waveforms have been band-pass filtered between 1 and 5 Hz. The color version of this figure is available only in the electronic edition.

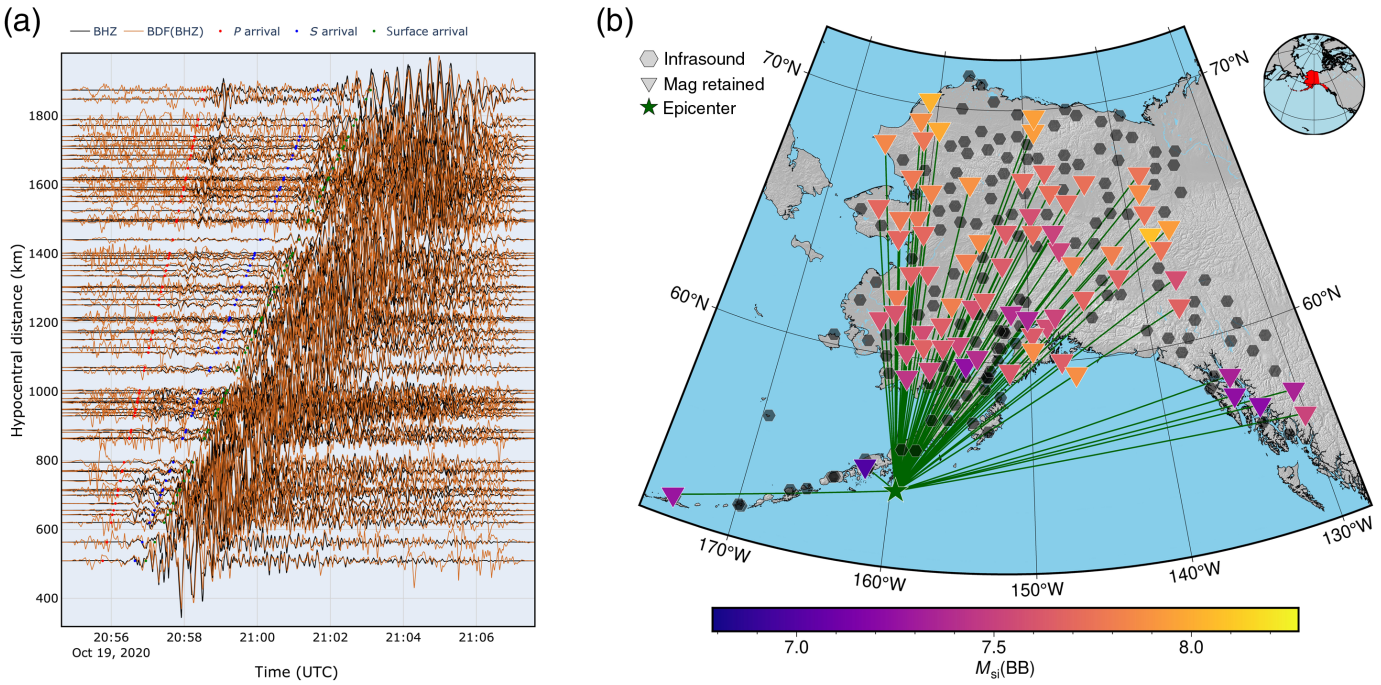

Figure 6. Broadband surface-wave magnitude results for the 19 October 2020 **M** 7.6 Sand Point earthquake. (a) The record section of waveforms from all stations that were used in the magnitude calculation. For each station, the vertical velocity from the broadband seismometer is shown in black, whereas the vertical velocity from the infrasound sensor is shown in brown. Stations are organized by hypocentral distance. (b) Infrasound stations used in the magnitude calculation are shown by inverted triangles colored by individual station magnitude. Gray hexagons denote available infrasound stations that did not record local infrasound adequately to estimate magnitude. The earthquake epicenter is from the Advanced National Seismic System (ANSS) catalog (U.S. Geological Survey, 2017). Inset at top right indicates the position of Alaska at a global scale. The color version of this figure is available only in the electronic edition.

estimate for 11 of the 12 stations. Although there is often strong-motion data available (e.g., RC01 is equipped with a strong-motion instrument), the integrations required to convert these data to velocity or displacement can be problematic if the ground motion has induced tilt, although this issue is more acute for horizontal channels (Melgar *et al.*, 2015). Even in the case of the largest earthquake we considered in this study, the great 29 July 2021 **M** 8.2 near Perryville—the nearest infrasound station, S15K, remained onscale at an epicentral distance of ≈111 km. This station recorded a peak pressure of just over 75 Pa. If we estimate the infrasound clipping level from the Mach number, the ratio of peak velocity to sound speed, then the 75 Pa value is well below the clipping level estimate of 100 Pa. Therefore, because the maximum amplitudes of the pressure perturbations associated with local infrasound are small, even for near-source stations and large earthquakes, CLI constitutes an essentially clipless and tiltless vertical seismic channel.

The results from our earthquake magnitude estimation shown in Table 2 indicate that robust earthquake magnitudes may be calculated from infrasound stations. Although our magnitude estimates from CLI underestimate the NEIC magnitude for the larger events (e.g., M_s_BB = 7.92 for the **M** 8.2 Perryville earthquake), the fact that there is generally good agreement between our magnitudes computed from seismic data and from CLI data indicate deficiencies in our magnitude estimators rather than with the use of CLI as the input data type. Seismic observatories routinely tune their algorithms to local conditions and networks, but no such tuning has been applied to our estimators. Further, we endeavored to compute magnitudes purely from infrasound, but clearly, infrasound could be combined with available seismic data to produce even more robust magnitude estimates.

It is clear from Figures 6 and 7 that even for large earthquakes that would be expected to generate high signal-to-noise ratios, only a subset of available stations record local infrasound that is highly correlated with collocated seismometers. As noted earlier, this is likely due to high noise levels at many of these stations. To quantify when a station is likely to record usable local infrasound without the need to refer to a collocated seismometer, we compared the pre-event noise, measured as the standard deviation of 5 min of data preceeding the *P*-wave arrival, with our calculated cross-correlation values. The result is shown in Figure 8a and indicates a reciprocal relationship between correlation and standard deviation. As expected, lower noise levels, as represented by lower standard deviations, result in higher correlations and more likely high-quality recordings of local infrasound. Somewhat surprisingly, Figure 8a indicates no relationship between station epicentral distances and correlation. To verify this, we also plot correlation as a function of source–receiver offset (see Fig. 8b), and this display does not indicate a dependence on distance, so that

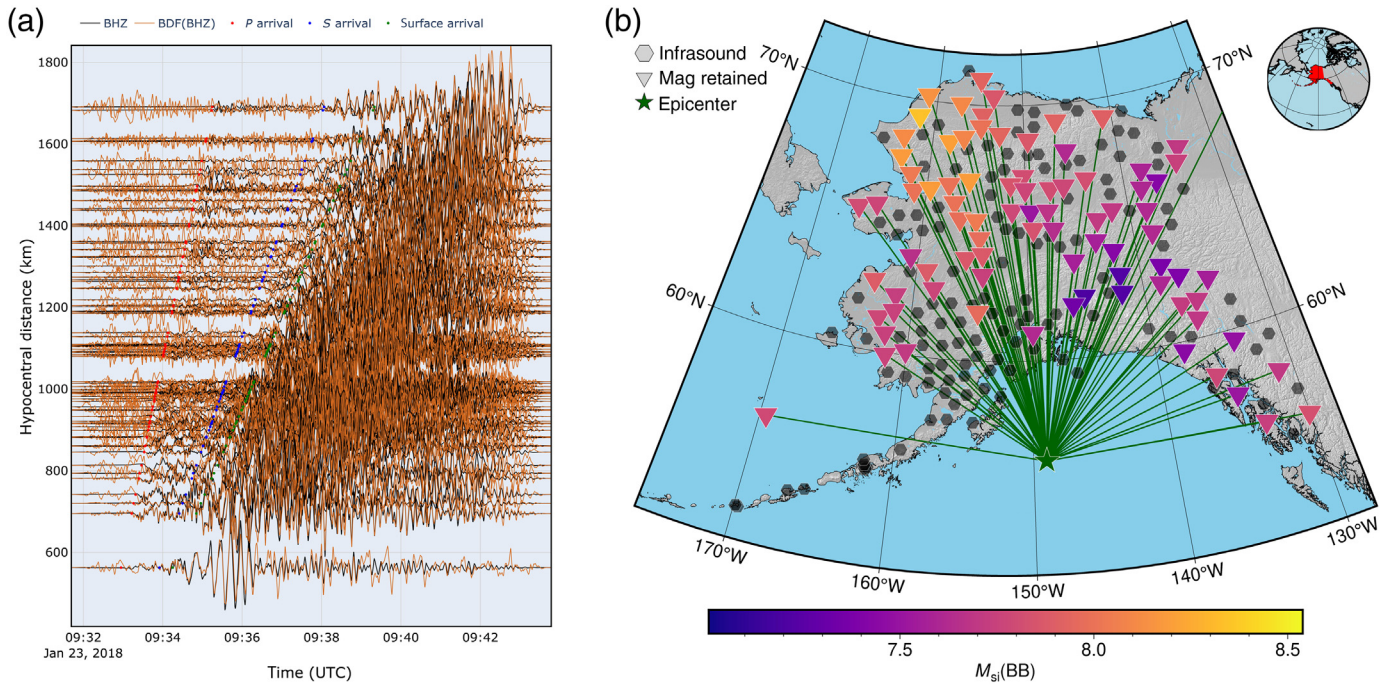

Figure 7. Broadband surface-wave magnitude results for the 23 January 2018 **M** 7.9 Kodiak earthquake. (a) The record section of waveforms from all stations that were used in the magnitude calculation. For each station, the vertical velocity from the broadband seismometer is shown in black, whereas the vertical velocity from the infrasound sensor is shown in brown. Stations are organized by hypocentral distance. (b) Infrasound stations used in the magnitude calculation are shown by inverted triangles colored by individual station magnitude. Gray hexagons denote available infrasound stations that did not record local infrasound adequately to estimate magnitude. The earthquake epicenter is from the ANSS catalog (U.S. Geological Survey, 2017). Inset at top right indicates the position of Alaska at a global scale. The color version of this figure is available only in the electronic edition.

the low pre-event noise is the most important criteria we found for predicting well-recorded local infrasound. To automate magnitude calculations from infrasound, more analysis will be required to define pre-event noise thresholds to aid decision making with respect to which stations to retain for use in the magnitude calculations.

A potential source of error in the magnitude calculations is the uncertainty in the acoustic parameters ρ and c in equation (2) that are used to compute the CLI. To evaluate the effect these values have on magnitude calculations, we recomputed the M_s(BB) for the Sand Point earthquake using extreme physical values for density and temperature. By assuming that temperatures between −50°C and 50°C, and densities between 1.1 and 1.6 kg/m^3 are close to the most extreme plausible values at ground level in Alaska, we determine the maximum and the minimum scaling values for equation (2). We then computed M_s(BB) values from amplitudes using these new conversion values. The results of this analysis for the Sand Point earthquake are shown in the scatter plot in Figure 9. Dots represent magnitudes presented above colored by the measured v_{max} value as a function of epicentral distance. Vertical bars for each value denote the magnitudes that would

TABLE 2
Magnitude Results for the Eight Earthquakes Considered in This Study

Earthquake	NEIC Magnitude	Magnitude (Seismic)	Magnitude (Infrasound)	Number of Stations	Magnitude Type
23 January 2018 Kodiak	7.9	7.69	7.78	85	M_s(BB)
12 August 2018 Kaktovik	6.4	6.32	6.40	38	M_{lv}
30 November 2018 Anchorage	7.1	7.02	7.04	47	M_s(BB)
22 July 2020 Perryville	7.8	7.63	7.70	44	M_s(BB)
19 October 2020 Sand Point	7.6	7.62	7.67	74	M_s(BB)
29 July 2021 Perryville	8.2	7.82	7.92	55	M_s(BB)
9 September 2022 Minto	3.7	3.89	4.09	Eight (single seismic)	M_{lv}
19 September 2022 Minto	4.9	4.84	4.98	Eight (single seismic)	M_{lv}

The published National Earthquake Information Center (NEIC) magnitude is from the Advanced National Seismic System (ANSS) catalog (U.S. Geological Survey, 2017), whereas the seismic and infrasound magnitudes are from this study.

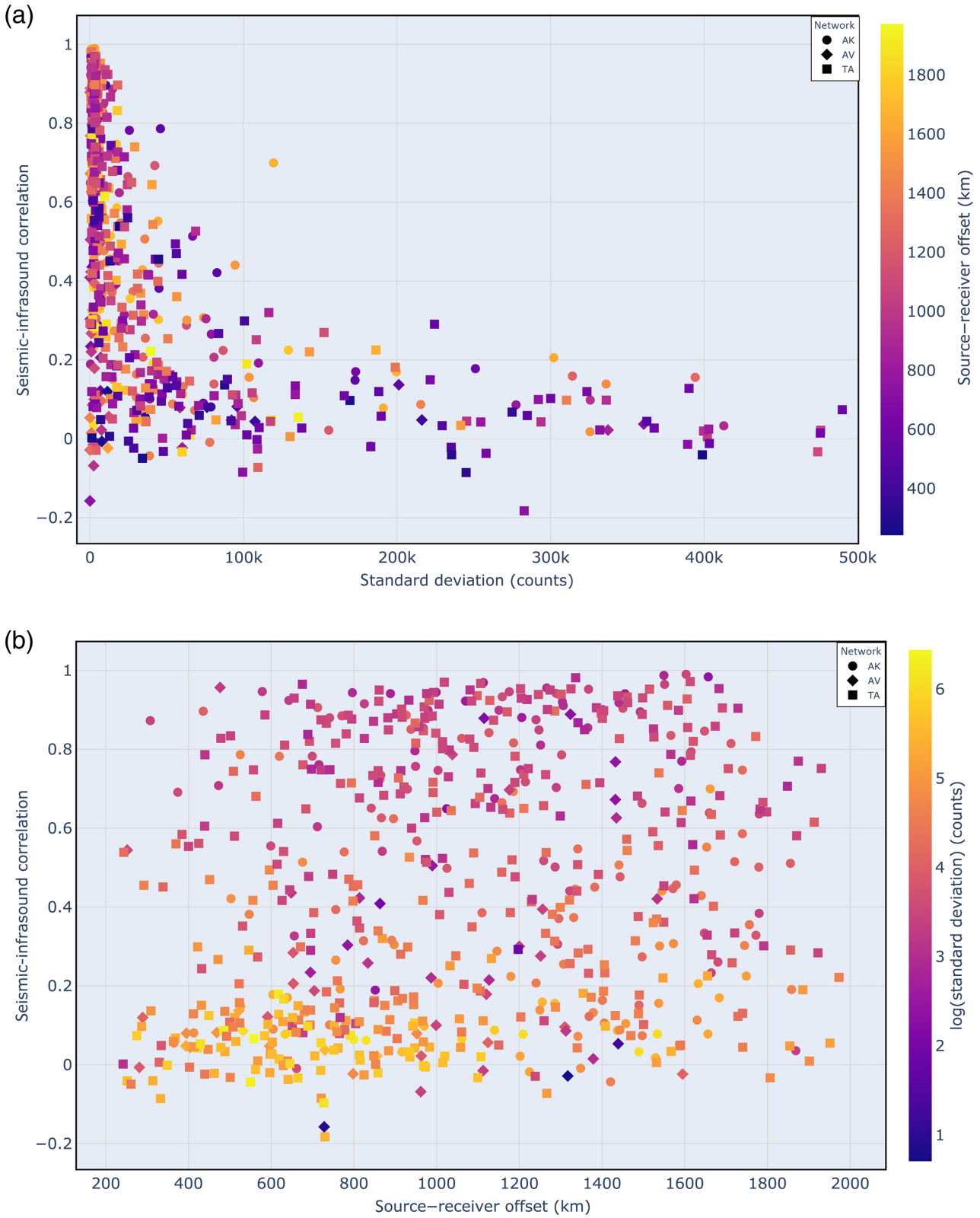

Figure 8. (a) Scatter plot of correlation as a function of pre-event noise. The pre-event noise is the standard deviation of five minutes of infrasound data preceding the predicted *P*-wave arrival. The correlation value is from cross correlating the converted infrasound waveform with the vertical seismic waveform. Circles, diamonds, and squares denote the AK, AV, and TA networks, respectively. Shapes are colored by station epicentral distance in kilometers. (b) Scatter plot of the same dataset as in panel (a) but with correlation as a function of epicentral distance. Shapes are colored by the log of pre-event noise and show that quieter stations have higher correlations with little relation to distance. The color version of this figure is available only in the electronic edition.

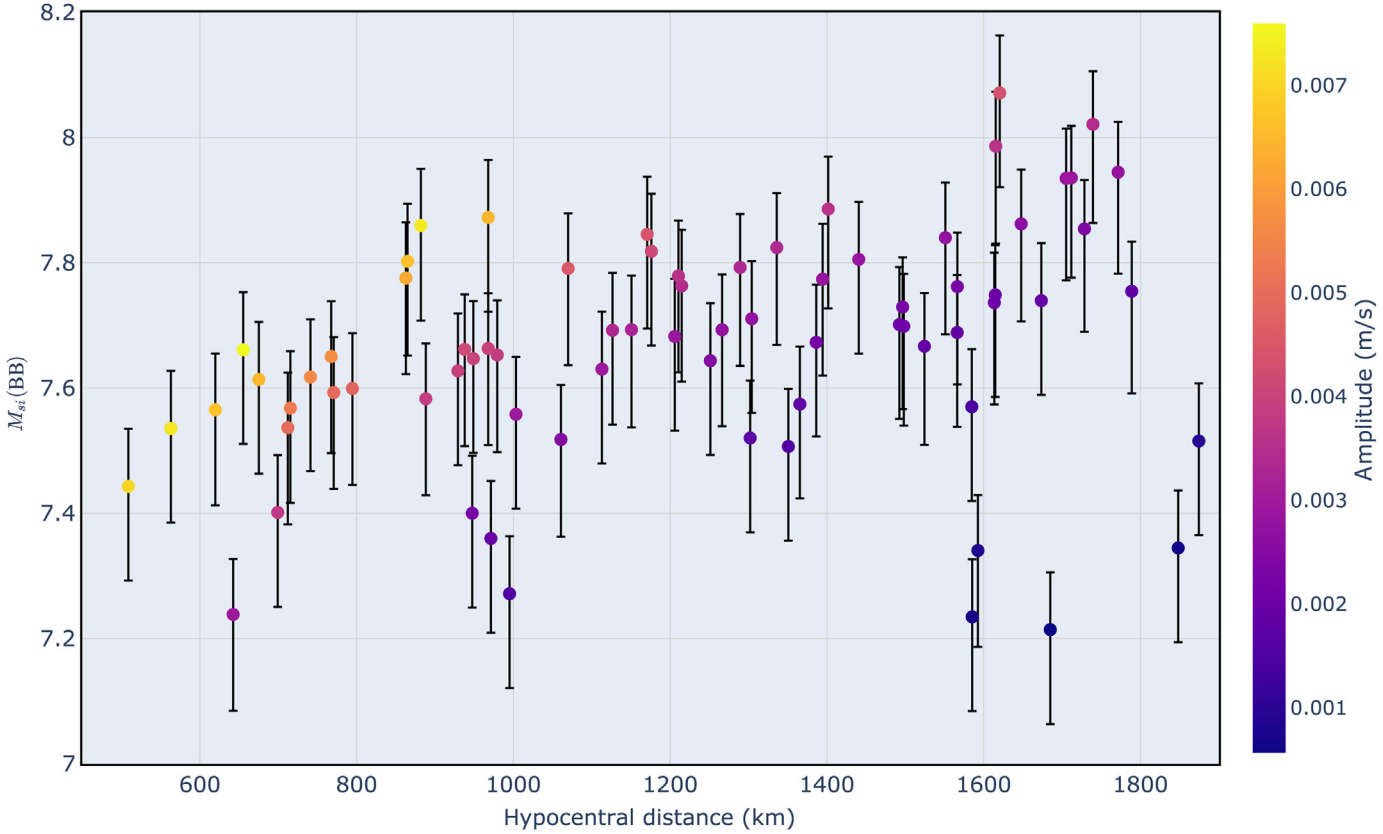

Figure 9. Scatter plot showing the range of M_s(BB) values for the **M** 7.6 Sand Point earthquake for each station that would occur if the pressure to vertical seismic velocity conversion was done using physically extreme values of acoustic parameters. Circles denote the preferred values used in the study and are colored by measured seismic velocity amplitude. Vertical lines at each point show the magnitude range imposed using the extreme values. The color version of this figure is available only in the electronic edition.

be determined, if the CLI conversion had used extreme physical values for the acoustic parameters. The plot indicates that using these extreme values would result in changing the magnitude estimate by plus or minus one or two-tenths of a magnitude. This indicates that determining extremely precise estimates of acoustic parameters is not required for accurate magnitude estimates.

CONCLUSIONS

We have demonstrated that the simple relationship between pressure perturbation and vertical ground motion may be used to convert local infrasound recordings of earthquakes to vertical seismic velocity that can then be used for earthquake source estimation. A feature of this technique is that absolute pressure amplitudes associated with local infrasound, even for large ground motions, are small, so that the vertical velocity recorded by infrasound sensors will rarely be subject to clipping or nonlinear effects for the maximum pressure values recorded for even great earthquakes. This technique will be useful for replacing broadband recordings of large and or near earthquakes that have clipped. Near-source recordings contain important information for many algorithms for estimating source parameters and are the stations most likely to clip. CLI can be used to replace clipped recordings for input into techniques including waveform inversion and fast magnitude estimators for earthquake early warning or tsunami warning.

We have also demonstrated that the CLI recordings may be used to estimate earthquake magnitudes. Our results show that the magnitudes can be calculated effectively using an infrasound array for a light local earthquake, allowing for an average magnitude value to be computed from the array. The CLI recordings are also viable for computing network magnitudes on a regional network for moderate-to-great earthquakes. Although this study was restricted to earthquakes, large subsurface explosions will also generate local infrasound, and the technique will be applicable to deriving magnitudes for such events or possibly for yield estimation (Stevens and Murphy, 2001). This study has focused on the M_{lv} and M_s(BB) magnitude estimators, but these are only proof-of-concept examples. Because CLI is effectively a vertical ground-motion time series, any algorithm that uses such seismic data will be able to leverage the infrasound recordings. This means that the local infrasound recordings become a viable data source for such tasks as tsunami warning, source inversions, or explosion monitoring.

Infrasound stations have become more ubiquitous in the recent years. Many former TA stations, with their single infrasound sensor, have been adopted into permanent regional networks, both in Alaska and in the conterminous United States.

The IM network includes a global grid of 53 infrasound arrays, with an eventual goal of 60 stations (Christie and Campus, 2010). Further, infrasound sensors are typically less expensive and easier to deploy than broadband seismic equipment. For example, a popular broadband instrument such as a Trillium 120 Posthole is factor of 2 more expensive than a current Hyperion infrasound sensor such as an IFS-5313. This study has demonstrated that infrasound has the potential to augment seismic data for some aspects of earthquake and seismic source monitoring using a readily available sensor platform.

DATA AND RESOURCES

All infrasound, seismic, and temperature data used in this study were produced by the networks of the USArray Transportable Array (TA) project (doi: 10.7914/SN/TA), the Alaska Earthquake Center (doi: 10.7914/SN/AK), Alaska Volcano Observatory (AV, doi: 10.7914/SN/AV), the Global Seismographic Network (GSN; doi: 10.7914/SN/II), and the International Miscellaneous Stations, and these data are available from the Incorporated Research Institutions for Seismology Data Management Center (IRIS DMC; http://ds.iris.edu/ds/nodes/dmc/, last accessed November 2022). This project relied heavily on free and open-source software packages including ObsPy (doi: 10.5281/zenodo.3706479) and PyGMT (doi: 10.5281/zenodo.5607255; Wessel *et al.*, 2019).

DECLARATION OF COMPETING INTERESTS

The authors acknowledge that there are no conflicts of interest recorded.

ACKNOWLEDGMENTS

The authors acknowledge the Alaska Native nations upon whose land our study area resides and note the stewardship of the traditional inhabitants of the region. This research was supported by the Defense Threat Reduction Agency Nuclear Arms Control Technology program under Contract Numbers HQ003421F0112 and HDTRA121C0030 (Distribution statement: Cleared for release); the operation and maintenance of many of the stations used in this study is supported by the National Science Foundation (NSF) Award Number 2024208. The authors thank two anonymous reviewers who made insightful comments and recommendations that improved the final article. The authors thank Tom Gabrielson and members of the Wilson Alaska Technical Center for helpful discussions in preparation of this article. The authors also thank Summer Ohlendorf at the U.S. National Tsunami Warning Center for discussions about broadband surface-wave magnitudes.

REFERENCES

Alaska Earthquake Center, University of Alaska Fairbanks (1987). Alaska regional network [data set], doi: 10.7914/SN/AK.

Alaska Volcano Observatory/USGS (1988). Alaska volcano observatory, doi: 10.7914/SN/AV.

Arrowsmith, S. J., R. Burlacu, K. Pankow, B. Stump, R. Stead, R. Whitaker, and C. Hayward (2012). A seismoacoustic study of the 2011 January 3 Circleville earthquake: Seismoacoustic study: Circleville earthquake, *Geophys. J. Int.* **189,** no. 2, 1148–1158, doi: 10.1111/j.1365-246X.2012.05420.x.

Bakun, W. H., and W. B. Joyner (1984). The ML scale in central California, *Bull. Seismol. Soc. Am.* **74,** no. 5, 1827–1843, doi: 10.1785/BSSA0740051827.

Beyreuther, M., R. Barsch, L. Krischer, T. Megies, Y. Behr, and J. Wassermann (2010). ObsPy: A Python toolbox for seismology, *Seismol. Res. Lett.* **81,** no. 3, 530–533, doi: 10.1785/gssrl.81.3.530.

Bormann, P., and J. W. Dewey (2012). The new IASPEI standards for determining magnitudes from digital data and their relation to classical magnitudes, in *New Manual of Seismological Observatory Practice 2 (NMSOP-2)*, P. Bormann (Editor), Deutsches GeoForschungsZentrum GFZ, Potsdam, Germany, 1–44.

Bormann, P., R. Liu, Z. Xu, K. Ren, L. Zhang, and S. Wendt (2009). First application of the new IASPEI teleseismic magnitude standards to data of the China national seismographic network, *Bull. Seismol. Soc. Am.* **99,** no. 3, 1868–1891, doi: 10.1785/0120080010.

Busby, R. W., and K. Aderhold (2020). The Alaska transportable array: As built, *Seismol. Res. Lett.* **91,** no. 6, 3017–3027, doi: 10.1785/0220200154.

Che, I.-Y., K. Kim, A. Le Pichon, J. Park, S. Arrowsmith, and B. Stump (2021). Illuminating the North Korean nuclear explosion test in 2017 using remote infrasound observations, *Geophys. J. Int.* **228,** no. 1, 308–315, doi: 10.1093/gji/ggab338.

Christie, D. R., and P. Campus (2010). The IMS infrasound network: Design and establishment of infrasound stations, in A. Le Pichon, E. Blanc, and A. Hauchecorne (Editors), *Infrasound Monitoring for Atmospheric Studies*, Springer Netherlands, Dordrecht, The Netherlands, 29–75, doi: 10.1007/978-1-4020-9508-5_2.

Cook, R. K. (1971). Infrasound radiated during the Montana earthquake of 1959 August 18, *Geophys. J. Roy. Astron. Soc.* **26,** nos. 1/4, 191–198, doi: 10.1111/j.1365-246X.1971.tb03393.x.

Crowell, B. W., and D. Melgar (2020). Slipping the Shumagin Gap: A kinematic coseismic and early afterslip model of the Mw 7.8 Simeonof Island, Alaska, Earthquake, *Geophys. Res. Lett.* **47,** no. 19, doi: 10.1029/2020GL090308.

Donn, W. L., and E. S. Posmentier (1964). Ground-coupled air waves from the Great Alaskan earthquake, *J. Geophys. Res.* **69,** no. 24, 5357–5361, doi: 10.1029/JZ069i024p05357.

Elliott, J. L., R. Grapenthin, R. M. Parameswaran, Z. Xiao, J. T. Freymueller, and L. Fusso (2022). Cascading rupture of a megathrust, *Sci. Adv.* **8,** no. 18, eabm4131 , doi: 10.1126/sciadv.abm4131.

Fee, D., K. Macpherson, and T. Gabrielson (2023). Characterizing infrasound station frequency response using large earthquakes and colocated seismometers, *Bull. Seismol. Soc. Am.* doi: 10.1785/0120220226.

Herman, M. W., and K. P. Furlong (2021). Triggering an unexpected earthquake in an uncoupled subduction zone, *Sci. Adv.* **7,** no. 13, eabf7590, doi: 10.1126/sciadv.abf7590.

IRIS Transportable Array (2003). Usarray transportable array [data set], doi: 10.7914/SN/TA.

Johnson, J. B., T. D. Mikesell, J. F. Anderson, and L. M. Liberty (2020). Mapping the sources of proximal earthquake infrasound, *Geophys. Res. Lett.* **47,** no. 23, e2020GL091421, doi: 10.1029/2020GL091421.

Kárník, V., N. V. Kondorskaya, J. V. Riznitchenko, E. F. Savarensky, S. L. Soloviev, N. V. Shebalin, J. Vanek, and A. Zátopek (1962). Standardization of the earthquake magnitude scale, *Stud. Geophys. Geod.* **6,** no. 1, 41–48, doi: 10.1007/BF02590040.

Kennett, B. L. N., and E. R. Engdahl (1991). Traveltimes for global earthquake location and phase identification, *Geophys. J. Int.* **105,** no. 2, 429–465.

Kim, T. S., C. Hayward, and B. Stump (2004). Local infrasound signals from the Tokachi-Oki earthquake, *Geophys. Res. Lett.* **31,** no. 20, doi: 10.1029/2004GL021178.

Kleckner, J. K., K. B. Withers, E. M. Thompson, J. M. Rekoske, E. Wolin, and M. P. Moschetti (2022). Automated detection of clipping in broadband earthquake records, *Seismol. Res. Lett.* **93,** no. 2A, 880–896, doi: 10.1785/0220210028.

Krabbenhoeft, A., R. von Huene, J. J. Miller, D. Lange, and F. Vera (2018). Strike-slip 23 January 2018 MW 7.9 Gulf of Alaska rare intraplate earthquake: Complex rupture of a fracture zone system, *Sci. Rep.* **8,** no. 1, doi: 10.1038/s41598-018-32071-4.

Krischer, L., T. Megies, R. Barsch, M. Beyreuther, T. Lecocq, C. Caudron, and J. Wassermann (2015). ObsPy: A bridge for seismology into the scientific Python ecosystem, *Comput. Sci. Discov.* **8,** no. 1, 014003, doi: 10.1088/1749-4699/8/1/014003.

Lay, T., and T. C. Wallace (1995). *Modern Global Seismology*, Academic Press, London, United Kingdom.

Lay, T., L. Ye, Y. Bai, K. F. Cheung, and H. Kanamori (2018). The 2018 M_w 7.9 Gulf of Alaska earthquake: Multiple fault rupture in the pacific plate, *Geophys. Res. Lett.* **45,** no. 18, 9542–9551, doi: 10.1029/2018GL079813.

Macpherson, K. A., J. R. Coffey, A. J. Witsil, D. Fee, S. Holtkamp, S. Dalton, H. McFarlin, and M. West (2022). Ambient infrasound noise, station performance, and their relation to land cover across Alaska, *Seismol. Res. Lett.* **93,** 2239–2258.

Melgar, D., B. W. Crowell, J. Geng, R. M. Allen, Y. Bock, S. Riquelme, E. M. Hill, M. Protti, and A. Ganas (2015). Earthquake magnitude calculation without saturation from the scaling of peak ground displacement: GPS PGD SCALING, *Geophys. Res. Lett.* **42,** no. 13, 5197–5205, doi: 10.1002/2015GL064278.

Melter, A., R. Rudnick, P. Zeitler, A. Levander, G. Humphreys, K. Karlstrom, G. Ekstrom, R. Carlson, T. Dixon, M. Gurnis, *et al.* (1999). USArray initiative, *GSA Today* **9,** no. 11, 40.

Richter, C. F. (1935). An instrumental earthquake magnitude scale, *Bull. Seismol. Soc. Am.* **25,** no. 1, 1–32, doi: 10.1785/BSSA0250010001.

Ruppert, N. A., C. Rollins, A. Zhang, L. Meng, S. G. Holtkamp, M. E. West, and J. T. Freymueller (2018). Complex faulting and triggered Rupture during the 2018 M_W7.9 Offshore Kodiak, Alaska, earthquake, *Geophys. Res. Lett.* **45,** no. 15, 7533–7541, doi: 10.1029/2018GL078931.

Scripps Institution of Oceanography (1986). Global seismograph network - IRIS/IDA, doi: 10.7914/SN/II.

Shani-Kadmiel, S., J. D. Assink, P. S. M. Smets, and L. G. Evers (2018). Seismoacoustic coupled signals from earthquakes in Central Italy: Epicentral and secondary sources of infrasound, *Geophys. Res. Lett.* **45,** no. 1, 427–435, doi: 10.1002/2017GL076125.

Stevens, J. L., and J. R. Murphy (2001). *Yield Estimation from Surface-Wave Amplitudes*, Birkhäuser Basel, Basel, Switzerland, 2227–2251, doi: 10.1007/978-3-0348-8310-8_13.

U.S. Geological Survey (2017). Advanced National Seismic System (ANSS) comprehensive catalog of earthquake events and products: Various, doi: 10.5066/F7MS3QZH.

Watada, S., T. Kunugi, K. Hirata, H. Sugioka, K. Nishida, S. Sekiguchi, J. Oikawa, Y. Tsuji, and H. Kanamori (2006). Atmospheric pressure change associated with the 2003 Tokachi-Oki earthquake, *Geophys. Res. Lett.* **33,** no. 24, doi: 10.1029/2006GL027967.

Wessel, P., J. F. Luis, L. Uieda, R. Scharroo, F. Wobbe, W. H. F. Smith, and D. Tian (2019). The generic mapping tools version 6, *Geochem. Geophys. Geosys.* **20,** no. 11, 5556–5564, doi: 10.1029/2019GC008515.

West, M. E., A. Bender, M. Gardine, L. Gardine, K. Gately, P. Haeussler, W. Hassan, F. Meyer, C. Richards, N. Ruppert, *et al.* (2020). The 30 November 2018 Mw 7.1 Anchorage Earthquake, *Seismol. Res. Lett.* **91,** no. 1, 66–84, doi: 10.1785/0220190176.

Xiao, Z., J. T. Freymueller, R. Grapenthin, J. L. Elliott, C. Drooff, and L. Fusso (2021). The deep Shumagin gap filled: Kinematic rupture model and slip budget analysis of the 2020 Mw 7.8 Simeonof earthquake constrained by GNSS, global seismic waveforms, and floating InSAR, *Earth Planet. Sci. Lett.* **576,** 117241, doi: 10.1016/j.epsl.2021.117241.

Xu, G., C. Xu, Y. Wen, W. Xiong, and S. Valkaniotis (2020). The complexity of the 2018 Kaktovik earthquake sequence in the Northeast of the Brooks Range, Alaska, *Geophys. Res. Lett.* **47,** no. 19, doi: 10.1029/2020GL088012.

Yang, M., T. Wang, and J. Shi (2021). Repeating infrasound from an earthquake doublet in Alaska, *Geophys. Res. Lett.* **48,** no. 17, doi: 10.1029/2021GL094632.

Zhang, J., J. Hao, X. Zhao, S. Wang, L. Zhao, W. Wang, and Z. Yao (2016). Restoration of clipped seismic waveforms using projection onto convex sets method, *Sci. Rep.* **6,** no. 1, 39056, doi: 10.1038/srep39056.

APPENDIX

This appendix provides plots of all waveforms used for magnitude calculations in the study. Figure A1 shows waveforms from the 23 January 2018 **M** 7.9 earthquake, Figure A2 the 12 August 2018 **M** 6.4 earthquake, Figure A3 the 30 November 2018 **M** 7.1 earthquake, Figure A4 the 22 July **M** 7.8 earthquake, Figure A5 the 19 October 2020 **M** 7.6 earthquake, Figure A6 the 29 July 2021 **M** 8.2 earthquake, and Figure A7 the 9 September 2022 **M** 3.9 earthquake.

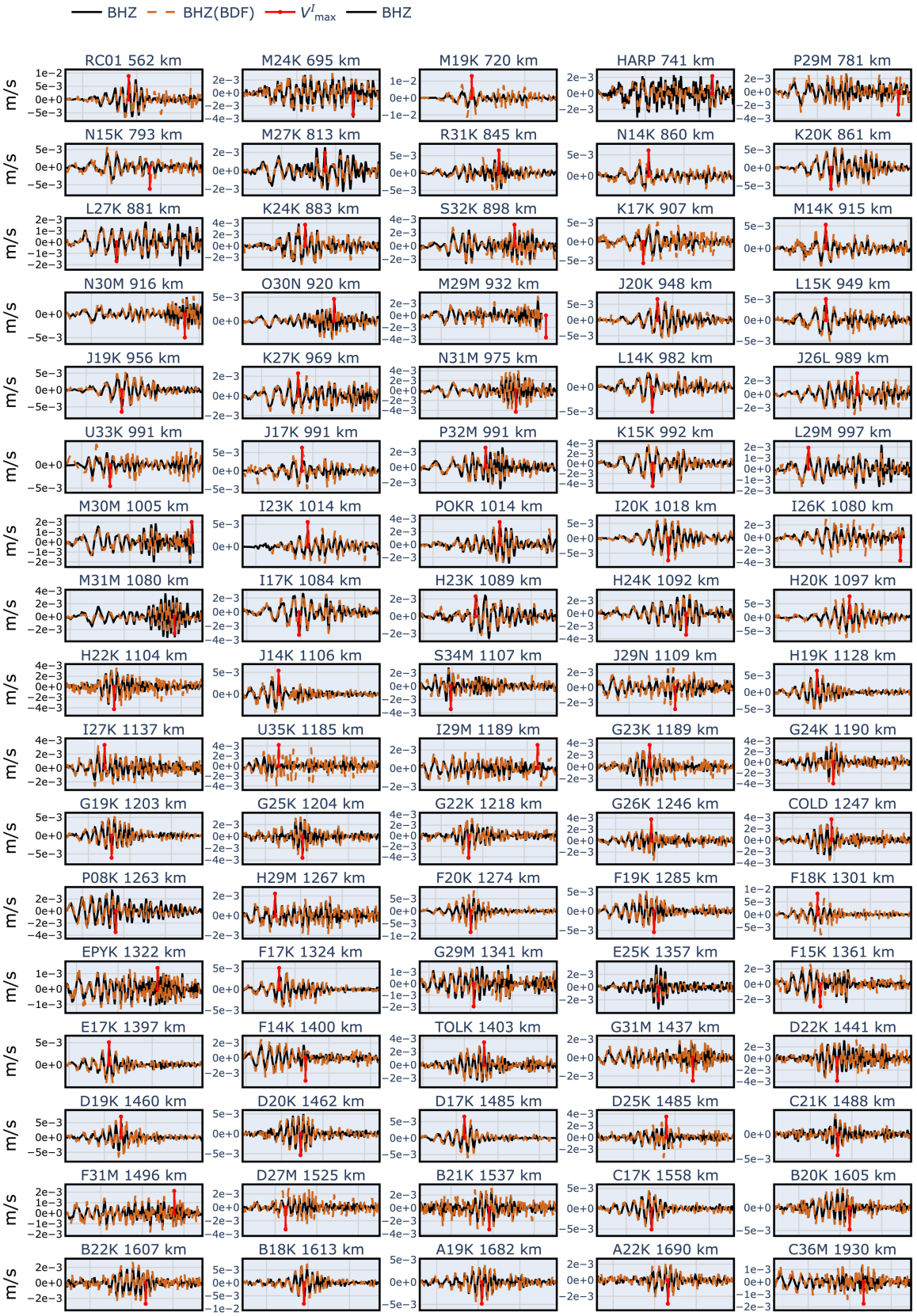

Figure A1. Waveforms for all stations used to compute magnitudes for 23 January 2018 **M** 7.9 earthquake. Vertical seismic velocity is shown in black, whereas CLI is shown is brown, both in meters per second. Waveforms have been moveout corrected by estimating the surface-wave arrival time, assuming a velocity of 3.5 km/s. Picks used for the amplitude measurement are shown as red vertical line segments. All waveforms have been band-pass filtered between 3 and 60 s. The color version of this figure is available only in the electronic edition.

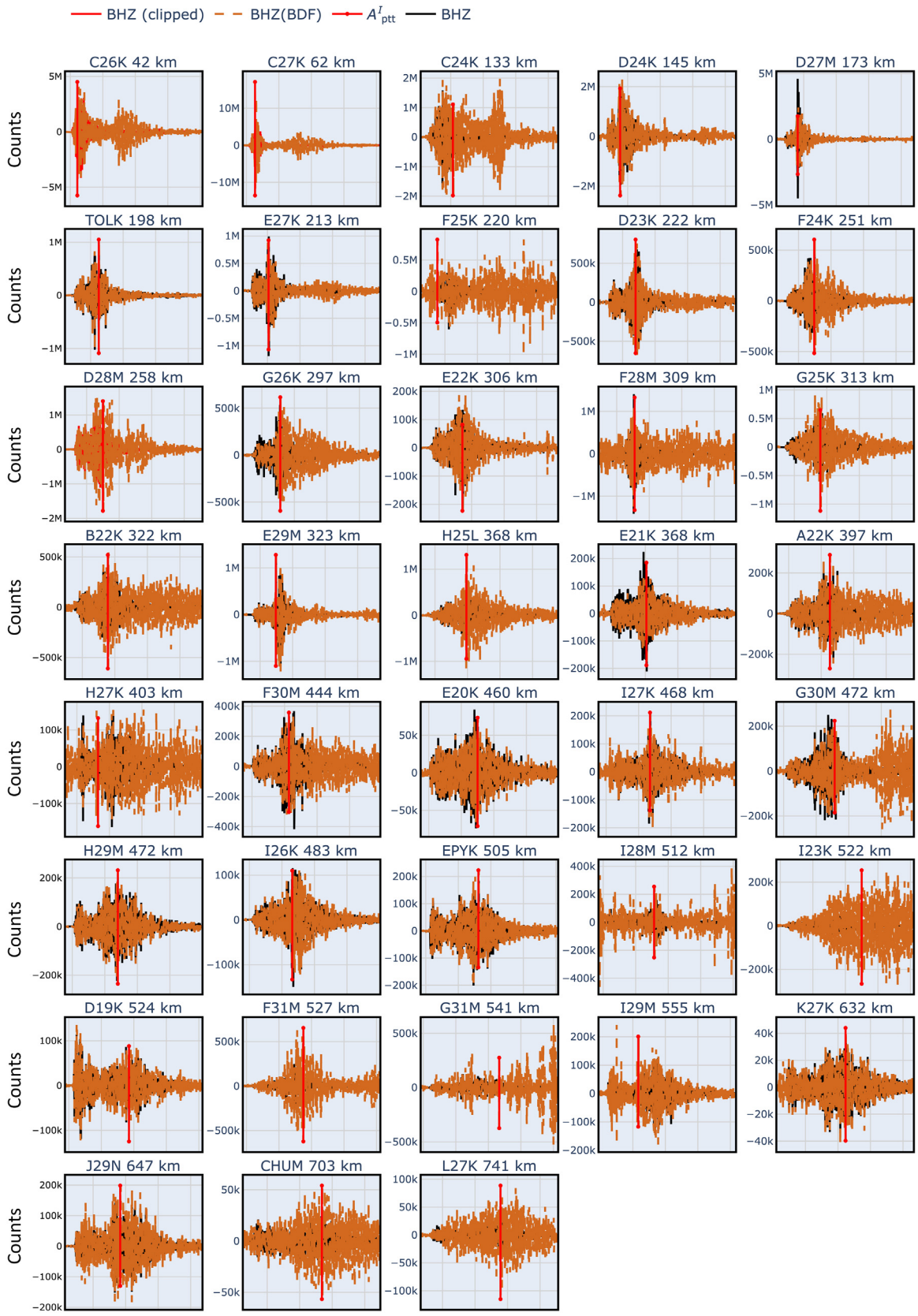

Figure A2. Waveforms for all stations used to compute magnitudes for 12 August 2018 **M** 6.4 earthquake. Vertical seismic velocity is shown in black, whereas CLI is shown is brown, both in counts. Waveforms have been moveout corrected by estimating the *P*-wave arrival time, assuming the IASP91 velocity model. Picks used for the amplitude measurement are shown as red vertical line segments. All waveforms have been band-pass filtered between 1 and 5 Hz. The color version of this figure is available only in the electronic edition.

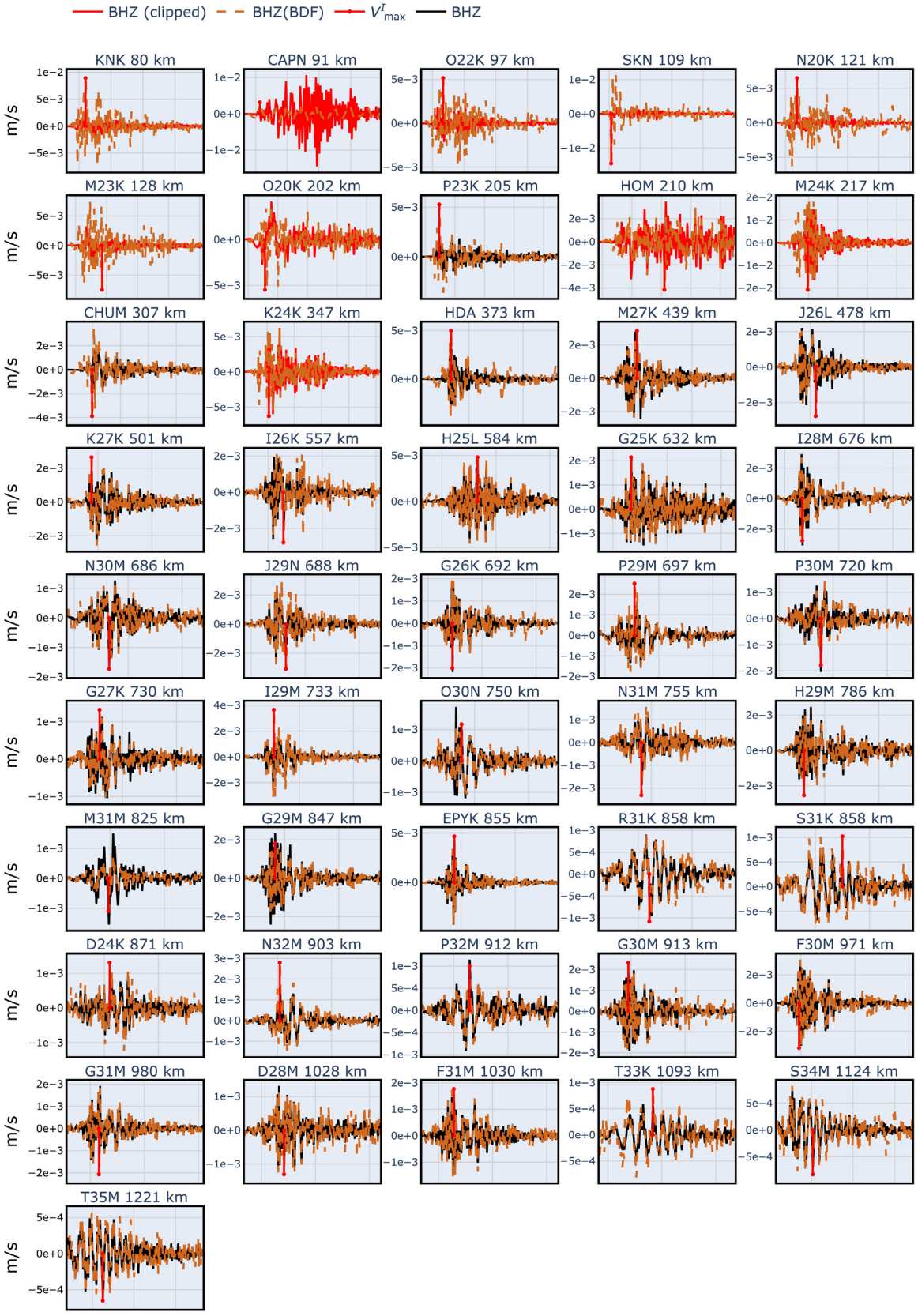

Figure A3. Waveforms for all stations used to compute magnitudes for 30 November 2018 **M** 7.1 earthquake. Vertical seismic velocity is shown in black, whereas CLI is shown is brown, both in meters per second. Waveforms have been moveout corrected by estimating the surface-wave arrival time, assuming a velocity of 3.5 km/s. Picks used for the amplitude measurement are shown as red vertical line segments. All waveforms have been band-pass filtered between 3 and 60 s. The color version of this figure is available only in the electronic edition.

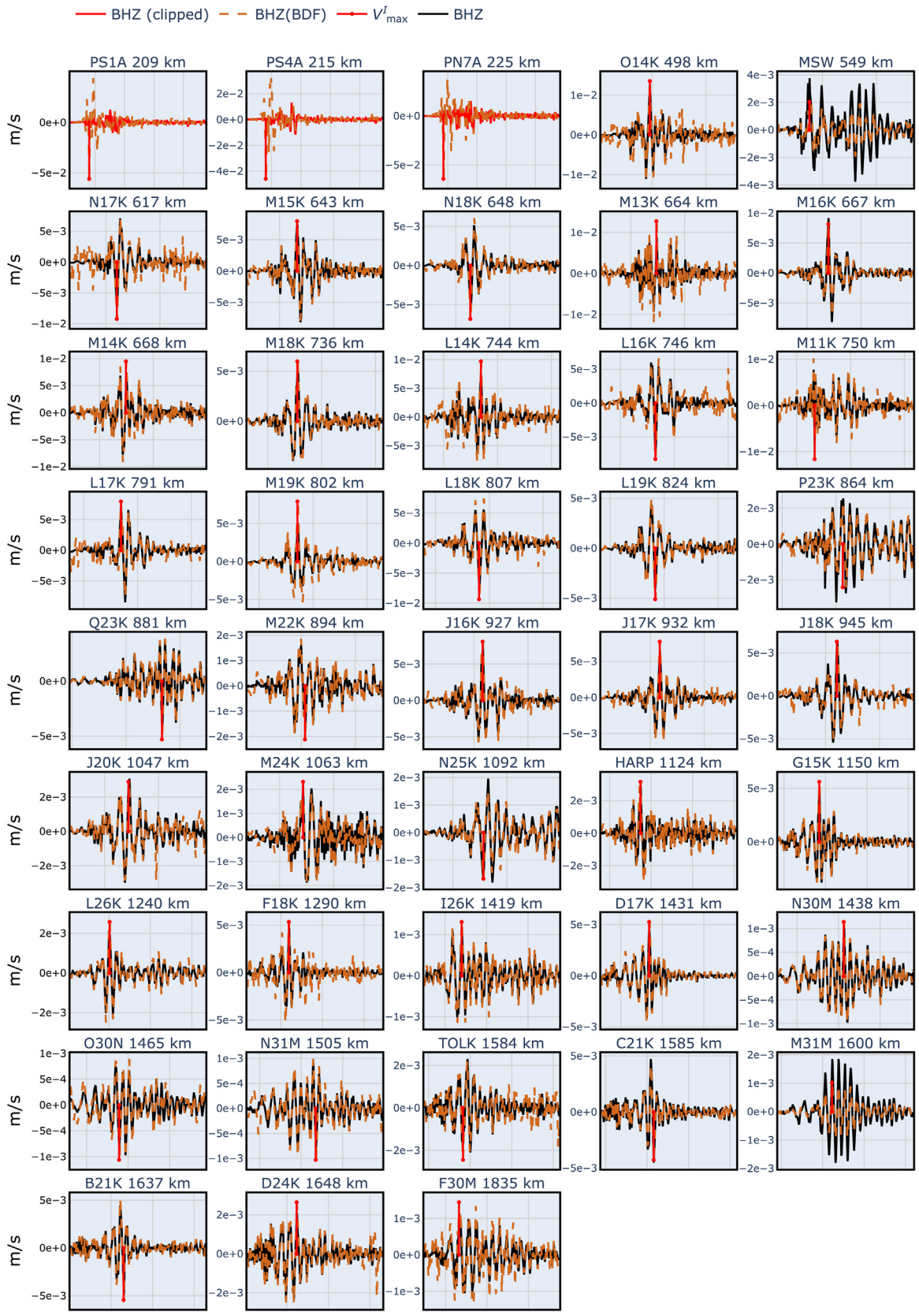

Figure A4. Waveforms for all stations used to compute magnitudes for 22 July 2020 **M** 7.8 earthquake. Vertical seismic velocity is shown in black, whereas CLI is shown is brown, both in meters per second. Waveforms have been move-out corrected by estimating the surface wave arrival time, assuming a velocity of 3.5 km/s. Picks used for the amplitude measurement are shown as red vertical line segments. All waveforms have been band-pass filtered between 3 and 60 s. The color version of this figure is available only in the electronic edition.

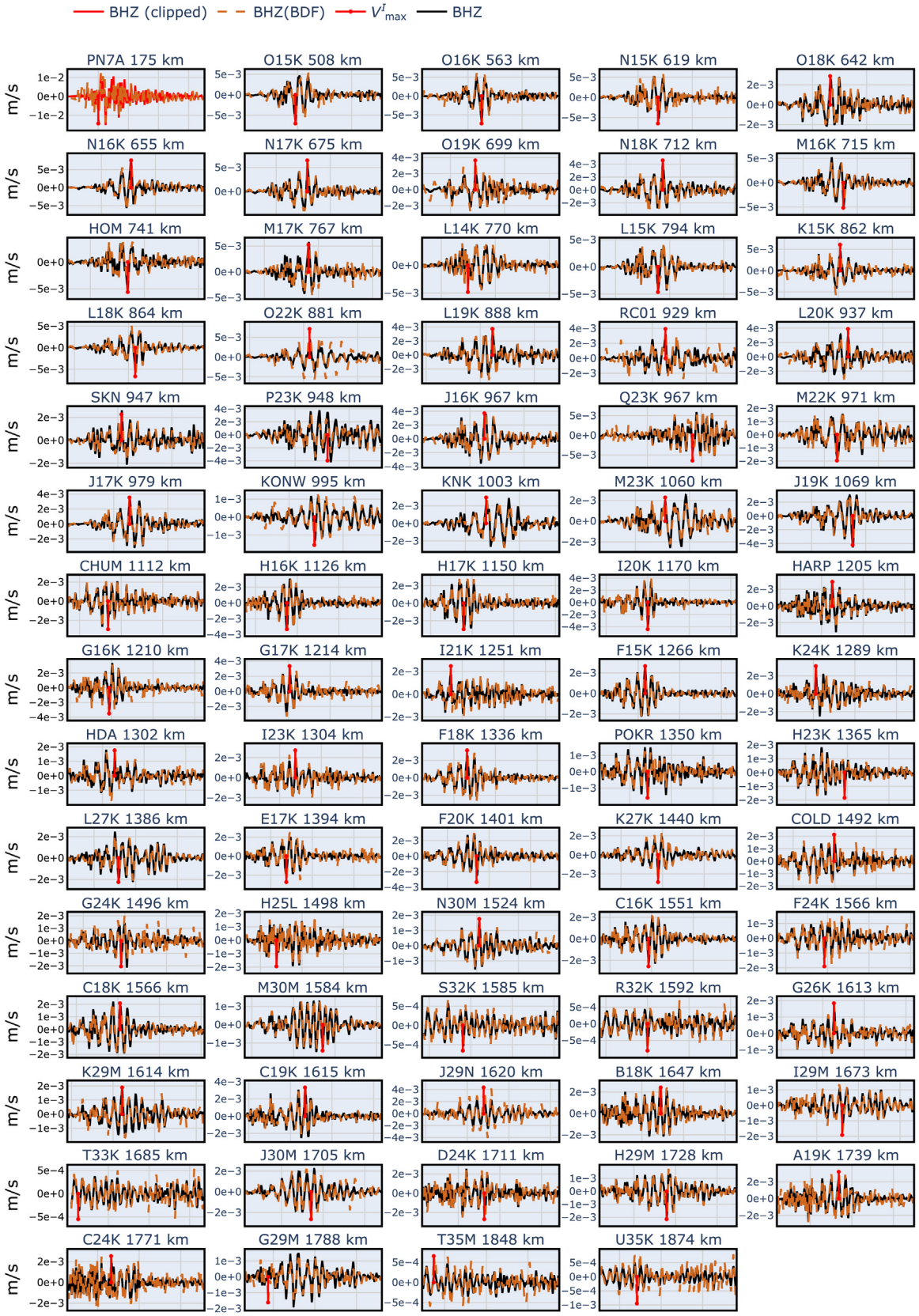

Figure A5. Waveforms for all stations used to compute magnitudes for 19 October 2020 **M** 7.6 earthquake. Vertical seismic velocity is shown in black, whereas CLI is shown is brown, both in meters per second. Waveforms have been moveout corrected by estimating the surface-wave arrival time, assuming a velocity of 3.5 km/s. Picks used for the amplitude measurement are shown as red vertical line segments. All the waveforms have been band-pass filtered between 3 and 60 s. The color version of this figure is available only in the electronic edition.

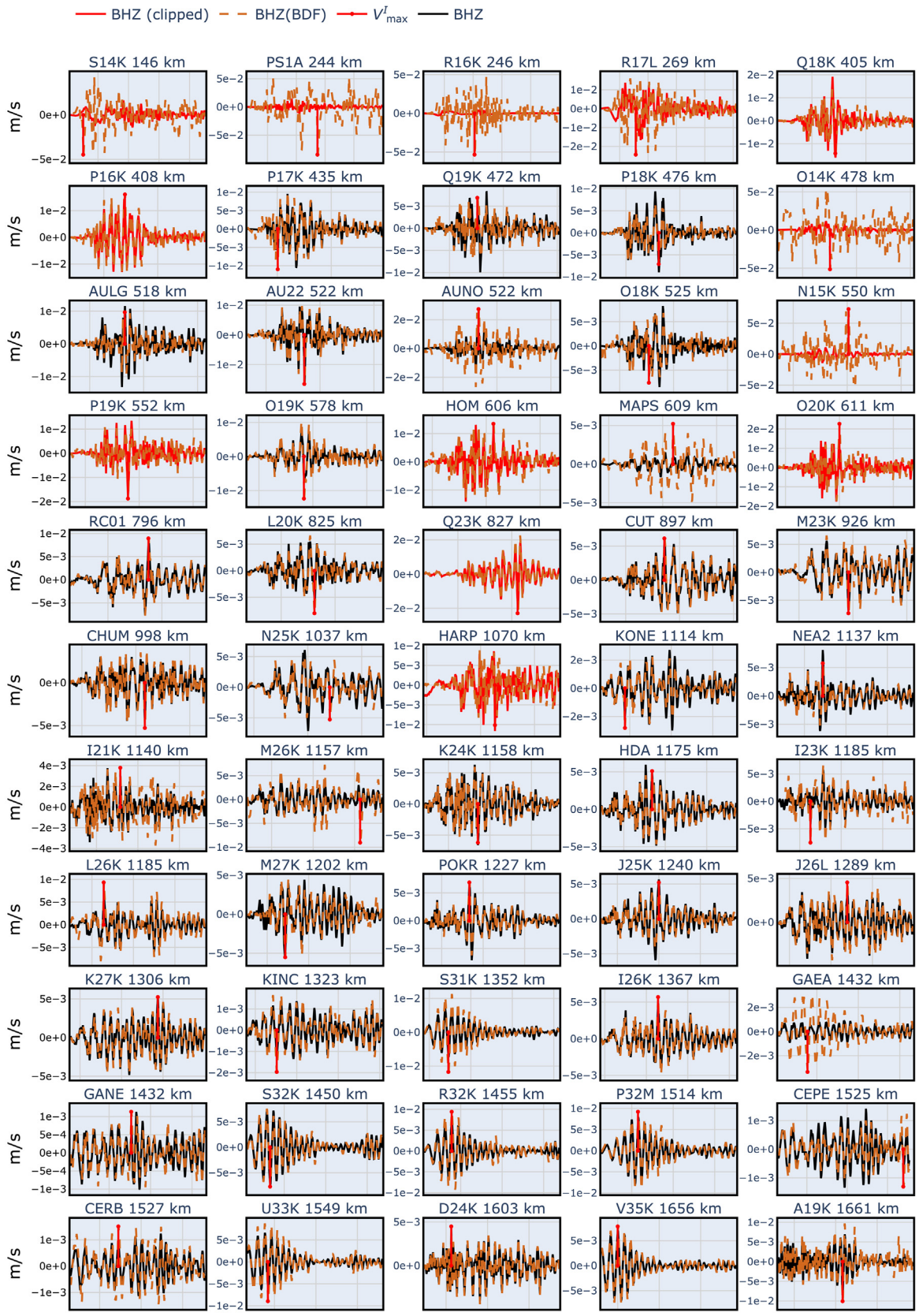

Figure A6. Waveforms for all stations used to compute magnitudes for 29 July 2021 **M** 8.2 earthquake. Vertical seismic velocity is shown in black, whereas CLI is shown is brown, both in meters per second. Waveforms have been moveout corrected by estimating the surface-wave arrival time, assuming a velocity of 3.5 km/s. Picks used for the amplitude measurement are shown as red vertical line segments. All waveforms have been band-pass filtered between 3 and 60 s. The color version of this figure is available only in the electronic edition.

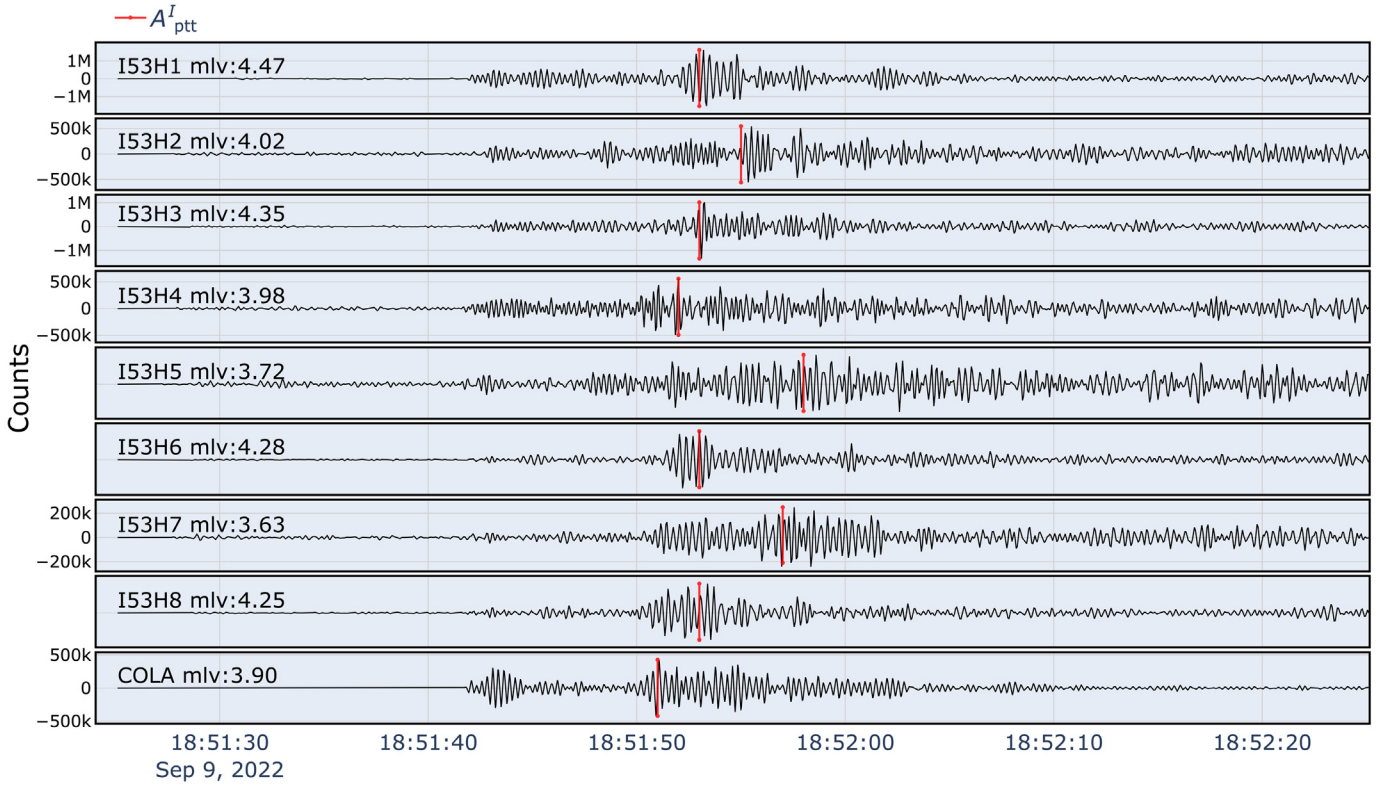

Figure A7. Waveforms for all stations used to compute magnitudes for 9 September 2022 **M** 3.9 earthquake. Vertical seismic velocity is shown in black, whereas CLI is shown is brown, both in counts. Waveforms have been moveout corrected by estimating the *P*-wave arrival time assuming the IASP91 velocity model. Picks used for the amplitude measurement are shown as red vertical line segments. All waveforms have been band-pass filtered between 1 and 5 Hz. The color version of this figure is available only in the electronic edition.

Manuscript received 15 November 2022
Published online 21 April 2023